ACS OMEGA

Open Access

http://pubs.acs.org/journal/acsodf

Article

Development of Novel Multifunctional Electroactive, Self-Healing, and Tissue Adhesive Scaffold To Accelerate Cutaneous Wound Healing and Hemostatic Materials

Asghar Khan, Wajid Rehman,* Mohammed M. Alanazi, Yaqoob Khan, Liaqat Rasheed, Abdul Saboor, and Shahid Iqbal

Cite This: *ACS Omega* 2023, 8, 39110−39134

Read Online

ACCESS | Metrics & More | Article Recommendations

ABSTRACT: Designing a multifunctional conducting hydrogel wound dressing of suitable mechanical properties, adhesiveness, self-healing, autolytic debridement, antibacterial properties, and radical scavenging ability, as well as retaining an appropriate level of moisture around the wound is highly desirable in clinical application for treating cutaneous wounds healing. Here, we designed a novel class of electroactive hydrogel based on thiol-functionalized silver-graphene oxide nanoparticles (GO/Ag/TGA) core polyaniline (PANI) shell GO/Ag/TGA/PANI nanocomposites. Thus, a series of physically cross-linked hydrogel based on GO/Ag/TGA/PANI and poly(vinyl alcohol) (PVA) was prepared by freeze−thawing method. The hydrogel was characterized by XRD, UV, FTIR, TGA, TEM, SEM, Raman spectroscopy, cyclic voltammetry (CV), and four probes test. The hydrogel showed favorable properties such as excellent tensile strength, suitable gelation time (30−56 s), tunable rheological properties ($G' \sim 1$ kPa), adhesiveness, and interconnected porous structure (freeze-dried). Besides this, the hydrogel also exhibits excellent exudate uptake capacity (10.4−0.2 g/g), high swelling ratio (72.4 to 93.5%), long-term antibacterial activity against multidrug-resistant (MDR) bacterial isolates, promising antioxidant (radical scavenging) efficiency, keeping the wound moisturized, prominent hemostatic efficiency, and fast self-healing ability to bear deformation. Interestingly, in vivo experiments indicated that electroactive hydrogels can significantly promote the healing rate of artificial wounds in rats, and histological analysis by H&E reveals higher granulation tissue thickness, collagen deposition, hair follicles, dermal papillary, keratinocytes, and marked increase ($P < 0.05$) in hydroxyproline at the wound site during 15 days of healing of impaired wounds. On the basis of vivo and vitro assay results, it is concluded that electroactive-hydrogel-attributed multifunctional properties may serve as suitable scaffold for treating chronic wound healing and skin regeneration.

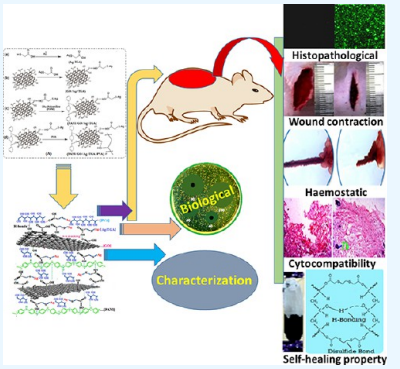

1. INTRODUCTION

In the human body, skin provides an effective barrier for protecting internal tissue from external damages such as physical and chemical factors, excessive temperature, and radioactivity and preventing body dehydration.[1] Once the damage of skin tissue occurs, the skin loses its protection mechanism, leading to severe wound infections, which present serious impact on health and threaten people's lives.[2] Therefore, the concept of wound treatment always focuses on minimizing potential environmental complications caused by the wound itself and enhancing proper regeneration of the wound skin tissue.[3] Recently, with the advancement of biomedical techniques, a wide range of biomaterials have been used for rapid wound healing including sponges, porous foam, electro-spun nanofibers, and polymeric hydrogels.[4] Among these materials, hydrogels have become a promising option[5] due to their natural porous structure, fast self-healing ability to bear deformation, ability to fill any irregular-shaped wound,[6] high water content to keep the wound moisturized, absorption of tissue exudates, gas exchange, and easy removal without trauma.[7] Hydrogels are three-dimensional networks of polymers and are classified as natural and synthetic according to their origin, and smart glues are synthetically prepared for the treatment of wounds.[8,9] Smart hydrogels show some unusual changes in their mechanical properties, network structure, and swelling behavior in response to different stimuli such as pH, temperature, ionic strength, as well as electric and magnetic field of the surroundings.[10] Besides physical protection of wounds, it is significant to develop strategies to design and construct hydrogel for active involvement in the healing process with outstanding mechanical behavior, electroactivity, elasticity,

Received: June 11, 2023
Accepted: September 29, 2023
Published: October 11, 2023

https://doi.org/10.1021/acsomega.3c04135
ACS Omega 2023, 8, 39110−39134

antimicrobial activity, antioxidant properties, and self-healing properties.

Conversely, a number of polymeric materials such as chitosan, cellulose, poly(vinyl alcohol) (PVA), and polyacrylate have been widely used in biomedical fields, particularly wound dressing applications.[11,12] Among them, poly(vinyl alcohol) (PVA) has drawn much attention for wound dressing applications due to its advantages such as being nontoxic, bioadhesive, and biocompatible and with high degree hydrolysis (>99%), low cost, biodegradability, and self-healing properties.[13] Additionally, physically cross-linking PVA hydrogels prepared by the freezing/thawing method also possess the ability of self-healing in air at room temperature without the need for any external stimulus or heating agents. The autonomous self-healing can be initiated due to the presence of free hydroxyl (OH) groups on the PVA chain on the cut surfaces prior to contact with hydrogen bonding with PVA chains in the hydrogel structure.[14] Moreover, PVA is also known as a metal stabilizer and is often used to synthesize hybrid nanocomposites for biomedical applications.[15] However, its application in the hydrogel form is not suitable for long-term applications under electrophysiological conditions due to their poor mechanical properties, less porosity, small equilibrium swelling ratio, and lack of multifunctional active involvement to accelerate tissue regeneration and the wound healing process.[16]

Recently, conducting hydrogels based on polypyrole (PPy), polythiophene, and polyaniline (PANI)[17] have been proven as one of the most promising synthetic extracellular matrix (ECM), possess intrinsic conductivity which regulates cellular activities including promoting cell adhesion, differentiation, proliferation, and migration of electrical-stimuli responsive cell such as fibroblasts,[18] stem cells,[19] nerve cells,[20] cardiac cells,[21] and direct the growth of a desired tissue.[5] Furthermore, skin is a kind of electrical signal-sensitive tissue that possesses its own conductivity values from 2.6 to 1×10^{-4} ms/cm.[22,23] It has been demonstrated that endogenous electric potential difference of 30∼100 mV/mm known as the trans epithelial potential (TEP) occurs naturally between the epidermis and dermis in the normal cavy and mammalian skin.[24] Another report demonstrates that in vivo around fresh wound 100∼200 mV/mm ionic current existed between the epidermises and stratum corneum and then slowly declined as the wound closed.[25] The TEP is known to occur as a result of accumulation of positive and negative charge (Na^+, K^+, Cl^-, Ca^{2+}, and ATPase) on the outside and inside of the epidermis, respectively. Disruption of these ionic currents and endogenous electric fields alters normal organ development, wound healing, and tissue regeneration.[26] These discoveries not only provide new insights regarding the endogenous electric field in biological tissue but also point to new directions for the therapeutic applications of electrical stimulation (ES) to accelerate wound healing through its effect on cell migration and protein synthesis,[27,28] even though the underlying mechanism remains unclear. Polyaniline (PANI) is a promising conductive polymer because of its convenient synthesis route, affordable cost, as well as its unique oxidation/reduction transition chemistry, and prominent electrical signal transmission has been abundantly used in biomedical applications.[29] Moreover, polyaniline could also regulate myogenic differentiation for muscle regeneration, enhancement of cell−cell interaction, and maturation of primary cardiomyocytes.[30] In addition, polyaniline scaffold also exhibits proper biocompatibility and milieu for L929 fibroblast and C_2Cl_2 myoblast cellular activity.[31] It has also been reported that vivo implantation of polyaniline scaffolds has resulted in poor biocompatibility toward certain types of cells such as NIH-$3T_3$ fibroblasts due to the remaining aniline monomers and oligomers during the polymerization of polyaniline and not because of the polymer itself.[32] However, the poor solubility and low mechanical properties of polyaniline hinder its wide application for long-term use as a wound dressing. Therefore, it is possible to add GO in hydrogel due to its superior electrical conductivity, porous structure, large water absorption, as well as high mechanical stiffness. However, some studies have pointed out that graphene oxide does not have antibacterial activity; therefore, in order to avoid wound infection at the wound site, some antibacterial agents like silver nanoparticles must be incorporated into the hydrogel due to its widespread antimicrobial spectrum. The graphene oxide and silver nanocomposites were further functionalized with mercapto acetic acid, which not only increases the GO/Ag nanocomposite interaction with the hydrogel and dispersibility but also increases adhesive properties of the hydrogel due to the presence of thiol groups on the surface of nanocomposites.

In this study, a facile approach has been developed for the fabrication of electroactive hydrogels based on GO/Ag/TGA/PANI (GATP) and (GATP-PVA) with desired multifunctional features, and we further demonstrated their potential to significantly promote the in vivo wound healing process in a full thickness skin model. For the preparation of this hydrogel, the GO/Ag/TGA (GAT) was first synthesized by direct deposition of silver nanoparticles (Ag-NPs) on the surface of graphene oxide (GO) in the presence of thioglycolic acid (TGA) to form GAT nanocomposites. PANI shell was formed over the surface of GAT nanocomposites by in situ chemical oxidation polymerization of aniline monomers to obtain GATP nanocomposites with the core−shell structure. In the last step, poly(vinyl alcohol) (PVA) was cross-linked with presynthesis GATP nanocomposites to obtain the final GATP-PVA hydrogel. The hydrogel was characterized with UV/vis, XRD, FTIR, TGA, SEM, TEM, and electrochemical measurement. The hydrogel exhibited excellent self-healing ability under multicyclic deformation, antibacterial property, antioxidant ability, efficient blood clotting capacity, good adhesiveness, high mechanical properties, improved conductivity, and good redox properties. All the data indicate that these hydrogels are very promising for use in biomedical applications, particularly as wound dressings.

2. RESULTS AND DISCUSSION

2.1. UV−visible Spectroscopic Analysis. In order to explore the adsorption of TGA on the surface of Ag-NPs, UV−visible analyses were used. Ag/TGA and pure Ag NP optical spectra in aqueous solutions are shown in Figure 1B. Further surface plasmon bonds and Ag-NPs larger than 2 nm normally have a strong and broad optical excitation peak in the UV−visible spectrum. Because Ag-NPs comparatively are unable to exhibit any peak, the UV−visible spectra of both Ag-NPs and Ag/TGA showed a uniform and homogeneous dispersion of nanoparticles in water. The surface plasmon bond peaks for Ag and Ag/TGA, respectively, were found at wavelengths of 316 and 418 nm, as shown in Figure 1B. The presence of a thiol group on the surface of Ag-NPs due to this redshift occurs in the position of the SPB peaks. It is also known that the SPB of metal depends on the size and size distribution of NPs, the larger the size of NPs, the higher the wavelength is as compared to those of smaller ones. The UV−vis result confirmed the existence of

https://doi.org/10.1021/acsomega.3c04135
ACS Omega 2023, 8, 39110−39134

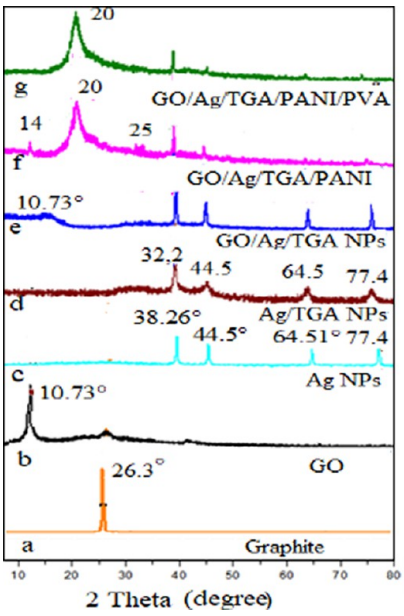

Figure 1. (A) X-ray diffraction patterns of (a) graphite, (b) GO, (c) Ag NPs, (d) Ag/TGA, (e) GAT, (f) GATP, and (g) GATP-PVA. (B) UV−visible spectroscopic analysis (a) Ag NPs and (b) Ag/TGA NPs. (C) Thermogravimetric curves of (a) GO, (b) PANI, (c) GATP, and (d) and GATP-PVA nanocomposites.

TGA on the surface of Ag NPs which shows consistency with the Raman result.

2.2. XRD Analysis. The formation of GATP-PVA-based hydrogels is confirmed through XRD patterns and shown in Figure 1A. The intensive peak of pristine graphite appears at around $2\theta = 26.23°$ interlayer spacing (0.34 nm) curve (a), while graphene oxide (GO) exhibited a sharp reflection peak at $2\theta = 10.73°$, corresponding to the (001) interlayer spacing (0.85 nm) which was much larger than that of pristine graphite due to the insertion of oxygen-containing functional groups on the graphite sheets. Curve (b). When compared with the unit cell of the face-centered-cubic (FCC) structure of metallic silver, Ag nanoparticles showed a sharp diffraction peak at various angles such as 38.26, 44.5, 64.51, and 77.47° with the Braggs reflections (111), (200), (220), and (311) and (JCPDS File No. 01−089−3722) Curve (c). The silver nanoparticles (Ag NPs) caped with the thiol group give a diffraction peak at the same 2θ value similar to pure Ag NPs but a slightly less intensive and broad peak as compared to the pure Ag NP Curve (d). The curve of Ag-based TGA analysis shows a less sensitive and broad peak than thioglycolic acid (TGA), confirming the formation of silver nanoparticles, slightly changing their crystallinity and face-centered cubic structure. For GAT, the characteristic peak of GO NPs becomes broader with the interplanar spacing (0.92 nm) slightly higher than GO NPs which demonstrates further reduction of GO during the reaction while the Ag/TGA peak becomes less intensive as compared to pure Ag nanoparticles curve (e). The GAT composite and GATP nanocomposites give broad and weak reflection at a 2θ value of 14.2, 20.4, and 25.1° corresponding to the periodicity parallel and perpendicular to the amorphous nature of polyaniline, and small peaks at the 2θ value of 38.26, 44.5, 64.51, and 77.47° indicate the existence of Ag NPs in nanocomposites, while the GO peak height that finally disappears in the composite might be due to the fact that the PANI polymer completely covered of the GO sheets to produce layered composites of GATP nanocomposites curve (f). The XRD peak of GATP-PVA nanocomposites presented a similar crystalline peak to that of pristine PANI but displays fewer and less intense peaks due to the high concentration of GO which reduces the intensity of PANI and Ag-NP reflection peak significantly curve (g).

2.3. Fourier Transform Infrared Spectroscopic (FTIR) Study. The chemical structure of GATP-PVA hydrogel was confirmed by the FTIR spectroscopy as shown in Figure 2. All of the other sample analyses were performed in the solid state except TGA because it was present in the liquid phase by using the KBr method. The assignments of bond and wavenumber are supported by the literature studies. There are various vibration and absorption peaks found in the pure spectra of TGA, which are due to asymmetric vas (OCO), symmetric s (OCO), symmetric (CO), symmetric (CH2), CC), and symmetric (OCO) vibrations, respectively, and two small peaks found at 2515 and 2541 cm^{-1} which belong to the S−H stretching bond. A strong OH band at 3413 cm^{-1} represents the presence of adsorbed water from the atmosphere. The GO nanosheet exhibited strong bands of C═O moieties (stretching vibrations from the carboxylic group at 1720 cm^{-1}), the O−H group (stretching vibration at 1335−1362 cm^{-1}), C═C (stretching vibration at 1620 cm^{-1}), epoxides (stretching vibration at 1210 cm^{-1}), and C−O−C units (stretching vibration at 1040−1120 cm^{-1}). Compared with pure TGA, the Ag-NPs/TGA show three absorption peaks at 1564, 1357, and 1250 cm^{-1} , and the corresponding thioglycolic acid carboxylate and alkoxy groups are confirmed to vibrate symmetrically and asymmetrically on the surface of silver nanoparticles, which is expected, given the structure of the covering layer. The distinct peaks at 3418 and 2969 cm^{-1} correspond with the −OH stretching mode due to the absorption of water and methylene groups, respectively. It can be seen that the characteristic peak of the S−H functional group is absent in Ag NPs/TGA and GO/Ag/TGA (GAT) and confirms the formation of a thiol group attached to the surface of Ag-NPs through the formation of Ag−S bonds. The addition peak at 2300 cm^{-1} is due to the CO_2 absorption band. Compared with GO, the absorption peak of GAT (stretching vibration at 1040−1210 cm^{-1} is relatively weak compared to those of GO which could be due to a lower degree of crystallinity. Figure 1C also demonstrates the FTIR spectra of GATP and GATP-PVA, respectively. The stretching vibrations of the benzenoid N−B−N (B: benzenoid unit) and quinonoid N═Q═N (Q: quinoide unit) show absorption peaks at ∼1557 and ∼1623 cm^{-1}. Peaks appear at wavenumbers of ∼1255−1230 cm^{-1} are assigned to the C−N^+ stretching and ∼1184−1175 cm^{-1} are assigned to the bending vibration of C−H stretching mode, respectively. The absorption peaks at ∼825−870 cm^{-1} are assigned to C−H of aromatic rings. The absorption band at ∼1047−1032 cm^{-1} is assigned to the sulfonate S═O− attached to the benzene ring of PANI. The peak at ∼520−650 cm^{-1} is assigned to aniline oligomers in nanocomposite structures. The presence of PVA in the GATP-PVA hydrogel was seen as strong absorption peaks at 3420, 2912, and 1465 cm^{-1} attributed to the OH stretching bend, C−H and CH_2 bonds, respectively. The spectrum of GATP-PVA shows all characteristic peaks similar to the GATP spectrum but less intensive, and the quinoide segment of PANI is slightly shifted from 1623 to 1638 cm^{-1} which indicates the presence of hydrogen bonding between PANI and PVA, and these results showed the presence of cross-link between GAT and GATP-PVA through the formation of the Schiff base and hydrogen bonding.

https://doi.org/10.1021/acsomega.3c04135
ACS Omega 2023, 8, 39110−39134

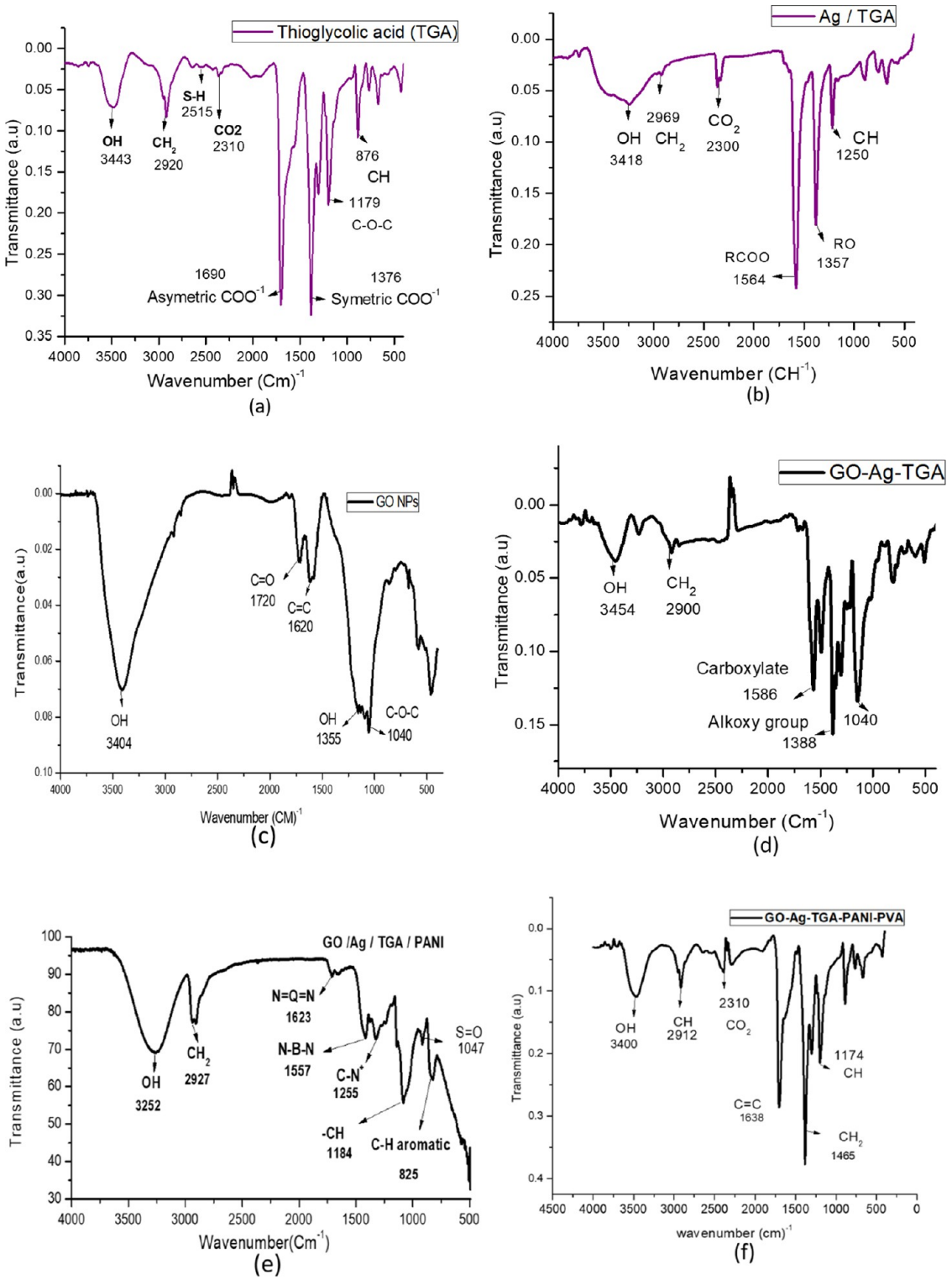

Figure 2. FTIR spectra of (a) TGA, (b) GO, (c) Ag/TGA, (d) GAT, (e) GATP, and (f) GATP-PVA nanocomposites using the KBR method.

2.4. Thermogravimetric Analysis. Thermal properties of the net GO, PANI, GATP, as well as GATP-PVA were studied by using a thermogravimetric analyzer, as shown in Figure 3. The thermal decomposing curve shows four distinct weight losses at the temperature range 70 to 100 °C, 140 to 180 °C, 230 to 350 °C, and 600 to 800 °C. The first weight loss occurred due to evaporation of deionized water which was attached to the intermolecular structure of the polymer, the second loss was due to dehydration etherification of PVA as well as a small amount of weight loss due to PANI oxidation, and the third loss was mainly the section of PANI thermal decomposing by releasing CO_2 and NH_3 gases while the fourth loss was due to carbonization of the polymer backbone. The net PANI shows one-step degradation starting at 230 to 310 °C attributed to the loss (26%) of the HCl dopant due to deprotonation of PANI. The GO shows two-step degradation; in the first step, at 93 °C, entrapped moisture is

https://doi.org/10.1021/acsomega.3c04135
ACS Omega 2023, 8, 39110−39134

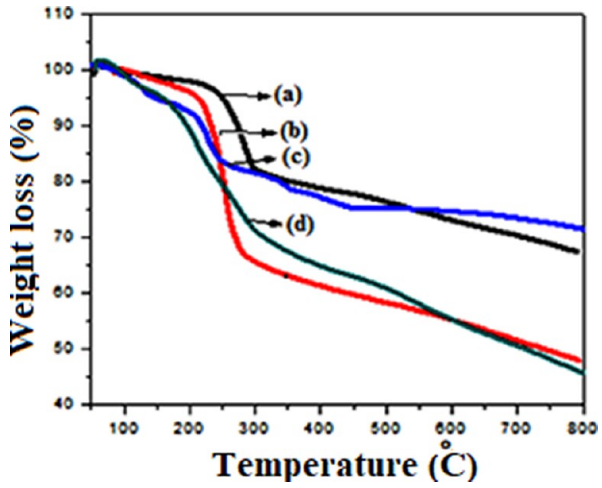

Figure 3. Thermogravimetric analysis of the prepared hydrogel.

removed, and in the second step, decomposition of oxygen-containing groups like carboxylic, hydroxyl, or epoxides groups present in the GO layers starts at 220 to 320 °C with 20% mass of GO is lost. Upon further increase of temperature up to 650 °C, no mass loss occurs while some of the GO changes to rGO, as reported elsewhere. Compared to pristine PANI and GO, it can be seen that there are four stages of weight loss that have been observed for the GATP and GATP-PVA nanocomposites. The first stage of weight loss occurs in the range 30−97 °C and is ascribed to the loss of moisture content, the second stage is attributed to dehydration etherification of PVA and decomposition of oxygen functional moieties from 120 to 180 °C, the third stage from 200−360 °C was mainly the degradation of different aliphatic and aromatic fragments of polyaniline nanocomposites with weight loss of 20−40% was estimated, and the fourth stage confirms the carbonization peak and temperature increase up to 600−800 °C, Furthermore, curve of thermogram slowly decrease and it is confirmed there is less effect of temperature on the loss of mass as well as the mass of residue tend to steady state. Overall the thermal stability of the GATP-PVA is enhanced ∼100 °C as compared to neat PANI with overall similar mass loss due to their strong physical bonding of GO layer with PANI nanocomposites. Moreover, it is also observed that GATP-PVA nanocomposites have 59.61% weight retention up to a temperature of 800 °C which could be attributed to good thermal stability of the nanocomposites.

2.5. Raman Spectra and SERS Activity of Nanocomposites. Typical Raman spectroscopic analyses were performed to elucidate the order and disordered insight of the crystal structure of carbon-based materials before and after the chemically stabilized Ag NPs absorbed on their surface. As shown in (Figure 4) the Raman spectra of GO exhibit two characteristic peaks: G band (the E_{2g} mode of sp^2 carbon atoms) at 1587 cm^{-1} and a D band (the symmetry A_{1g} mode) at 1378 cm^{-1} that corresponds to defects or edge areas. The ratio of D/G intensity of GO was 0.914. It can also be observed that the intensities of these two bands were enhanced dramatically after the decoration of Ag-NPs and Ag/TGA NPs on the GO surface but the ratio of D/G did not change significantly. Simultaneously, we also observed several vibration absorption peaks of TGA adsorbed on the surface of Ag-NPs at 1682,1388, 1080, 989, 840, 765, and 695 cm^{-1} which are caused by $\nu(-CO)$, s(OCO), s(CC), $\nu(CC)$, $\rho(CH2)$, $\nu(CS)$, and $\delta(OCO)$ vibrations, respectively. In addition to these bands, the Raman spectra of GAT also contain bands at lower wavenumbers (587, 757, and 973 cm^{-1}) which showed a typical indication of a strong interaction between the S atom and Ag-NPs and are joined with the (CCO), (C−S), and (CC) stretching vibration of TGA. Hence, a proposed model showing the possible chemical attraction ($\pi-\pi$ stacking, electrostatic interactions, and hydrogen bonding) between the GAT NPs is displayed in Figure 4A. We also observed other Raman emission bands assigned to the functional group of PANI at 1173 cm^{-1} (C−H bending vibration of the benzenoid ring), 1236 cm^{-1} (symmetric C−N stretching of the benzenoid ring), 1363 cm^{-1} (−C−N^+ vibration of the delocalized polaronic structure), 1476 cm^{-1} (C═N stretching of the quinoide ring), 1580 cm^{-1} (C═C stretching of the quinoide ring) in synthesized GATP nanocomposites Figure 4.

The assignment of Raman peaks is in good agreement with previous reports confirming that the synthesized product contains polyaniline. It is noteworthy that the C−N stretching of the benzenoid ring and the C═N stretching of the quinoide ring at 1236 and 1476 cm^{-1} are slightly shifted toward lower wavenumbers (1227 and 1463 cm^{-1}) in the case of GATP-PVA, reconfirming the interactions between the GATP with PVA hydrogel (Table 1). These phenomena were also observed in a previous report. The peaks at 2937 cm^{-1} can be assigned the presence of methylene (CH_2) or methyl (CH) groups. Intriguingly, GAT shows the comparison of SERS activity with GO/Ag NPs due to TGA absorbed on the Ag-NPs and enhances the electromagnetic fields on the surface plasmon resonance, and charge transfer between the Fermi levels of the Ag/TGA NPs increases the molecular Raman signal by many orders of magnitude. All of these results reveal that GAT dopes on the quinoide ring of PANI due to the proton doping mechanism of PANI and the presence of the carboxyl group on the GO surface and TGA to form a conductive GATP composite.

2.6. Surface Morphology (SEM). The surface morphology of these GAP-PVA and GATP-PVA hydrogels was observed with a scanning electron microscope (SEM). As shown in Figure 5A−D, the surface of hydrogel exhibits a rough, wiggled, wrinkled, packed lamellar, and porous shape, which is confirmed through the intermolecular and intramolecular cross-link structure due to the presence of carboxylic and thiol groups. The spherical-shaped granules can be observed on the surface of the PVA polymer, with diameters ranging from 0.4 to 1 μm (Figure 5A). The GAT acts as a template, and PANI is proven on the surface of GO due to the presence of electrostatic force and hydrogen bonding between the PANI and GAT (Figure 5B). The hydrogel pore size was in inverse relation to the weight ratio of GATP shown in Figure 5C,D that higher GATP mass ratios resulted in smaller hydrogel pore sizes, which minimized porosity. The pore size of the hydrogel gradually decreases from 87.3 to 65.2% as the ratio of the GATP nanocomposite increases from 0−10 wt %. The pore diameter of GATP-PVA is estimated to be 4−7 μm which gradually decreases along with an increase in GATP nanocomposite. The decrease in the porosity of the hydrogel seems to be due to the formation of strong cross-link density between the nanocomposite and matrix, tending to decrease the size interconnecting pore and capillary structure. Due to their greater number of pores and high cross-linking properties, the obtained hydrogel is supposed to be used for biomedical applications, including tissue engineering, as hemostatic agent, and drug delivery.

2.7. TEM Observations. The morphology of the nanocomposites was studied by using transmission electron

https://doi.org/10.1021/acsomega.3c04135
ACS Omega 2023, 8, 39110−39134

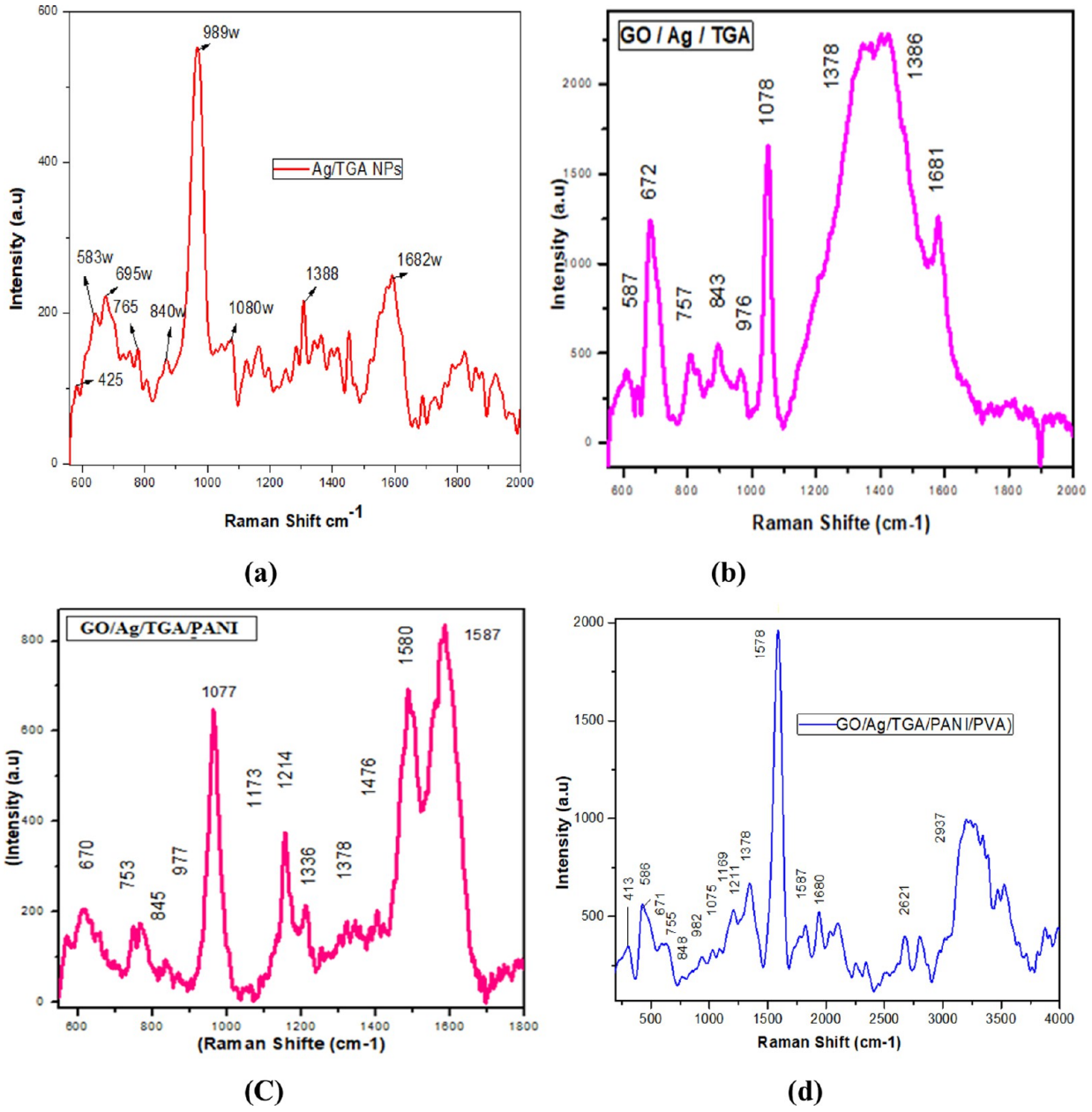

Figure 4. (a−d) Raman characterization and SERS activity of GO, GO/Ag, GO/A/TGA and GATP, GAP-PVA, and GATP-PVA hydrogels.

microscopy (TEM). As can be seen in Figure 6a, GO exhibited a thin nearly transparent sheet with a leaflike vein structure that came from the crumpling and scrolling of graphene sheets during the oxidation process. TEM images of GAT in Figure 6b,c at different magnifications showed a uniform deposition of Ag NPs as dark nearly spherical spots on the surface of GO sheets with a size of about 15−20 nm with less agglomeration and showed a quite strong interaction between the Ag NPs and GO sheets due to two reasons. First, due to the surface modification of Ag NPs with thiol groups and the presence of a −COOH functional group on the GO frameworks, which act as chemically active sites for the interaction of Ag-NPs with the −COOH group of GO sheets. Second, the mechanisms of interaction between GO and Ag-NPs are van der Waals force and pi−pi stacking as Ag-NPs enter the interlayer space of GO sheets. TEM images of the GATP composite (Figure 6d,e) show an inner black layer of GO sheets and the outer wrinkled wavy shape of PANI on its surface to form a crumpled paper-like structure; these wavy wrinkles interpreted physical adsorption of PANI nanoparticles on GO sheet's surface due to $\pi-\pi$ interaction force that was explicated by Raman analysis. In addition, the TEM result of GATP-PVA shows a homogeneous codispersion of GATP with PVA which could lead to enhanced interfacial adhesion and mechanical performance of the nanocomposites.

2.8. Self-Healing Property of the Hydrogel. Hydrogels with the ability to self-heal can prolong the lifespan of the wound dressing and provide better wound protection. To assess the self-healing properties of the hydrogel, a rheological recovery test was performed. The strain amplitude sweep test at a constant frequency of 10 rad s^{-1} at 25 °C was first performed up to the critical point which is the state of the hydrogel, which is solid or fluid, as shown in Figure 7a, in the early stage of curing storage modulus (G') is greater than loss modulus (G'') which endorses

https://doi.org/10.1021/acsomega.3c04135
ACS Omega 2023, 8, 39110−39134

Table 1. Raman Dates, SERS, and Assigned Observe Mode[a]

mode	A/T (cm^{-1})[b]	GAT (cm^{-1})[b]	GATP (cm^{-1})[b]	GATPP (cm^{-1})[b]	assignment[c]
Q1	425vw	417w	415w	413w	δ (CCO)/p(OCO)
Q2	583w	587s	589s	586s	s (C−S + C−C)
Q3	695w	672m	670m	671m	δ (OCO)
Q4	765w	757w	753m	755m	(CS)
Q5	840w	843w	845m	848m	P (CH_2)
Q6	989w	976s	977s	982s	ν (CC)
Q7	1080w	1078s	1077w	1075m	s (−C−C)
Q8			1173w	1169w	(C−H benzenoid ring)
Q9		1217w	1214w	1211w	w (CH2)
Q10			1236s	1227s	s (C−N stretching of benzenoid ring)
Q11			1363s	1361s	s (−C−N^+)
Q12		1378w	1378vs	1378s	D 9GO)
Q13	1388w	1386m	1383m	1384m	νs (OCO)
Q14			1476w	1463w	s (C═N of quinide ring)
Q15			1587w	1587w	G (C═O of GO)
Q16			1580vs	1578vs	S (C═C stretching of quinoid ring
Q17	1682w	1681w	1679s	1680s	ν (C═O of TGA)
Q18			2623s	2621s	D+G (GO)
Q19				2937s	νs (CH_2)

[a]Abbreviations: AT, Ag/TGA; GAT, GO/Ag/TGA; GATP, GO/Ag/TGA/PANI; GATPP, GO/Ag/TGA/PANI/PVA. [b]Relative intensity: s, vs, and vw means strong, very strong, and very weak. [c]The Raman observed shifts are shown; ν, in-plane stretching; δ, in-plane bending; γ, out-of-plane bending; w, wagging; ρ, rocking; s, symmetric; t, twisting; and as, asymmetric.

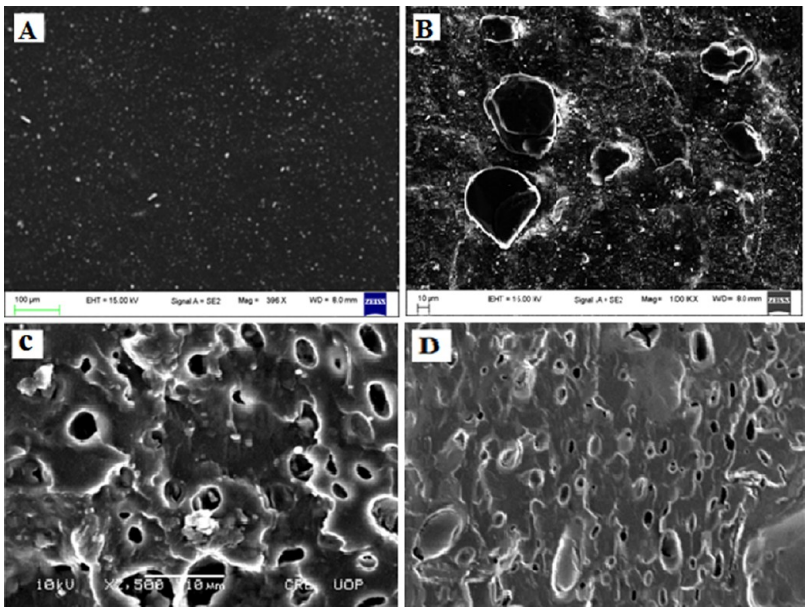

Figure 5. Cross-sectional morphology of GATP-PVA gel (A, B) and GAP-PVA gel (C, D), both prepared at 10% (w/v) concentration, is shown in the SEM images.

the features of a stable hydrogel network. At high shear strain amplitude, the viscous component (G'') overcomes the elastic modulus curve (G') at 260% strain referring to the cross-over strain or critical point. This critical point signifies a very important physical parameter such as the transition from viscous elastic solid to viscoelastic liquid, revealing the collapse of the hydrogel network. The hydrological recovery test of the hydrogel was performed by a continuous step strain method, as shown in Figure 7e. When the hydrogel was further subjected by applying a strain of about 500%, the G' value dropped from 221 to 7 Pa. The value of G' however, returned to the initial stage once the strain was reduced to 1%. The hydrogel's ability to alternately exhibit breaking and recovery behavior a number of times confirms that it has a highly effective and quick self-healing capability. The variation of the value of storage modulus (G') and loss modulus (G'') with shear stress at a constant frequency of 10 rad s^{-1} at 25 °C are also given in Figure 7b. The hydrogel capacity for self-healing was magnified even further. First, two pieces of the hydrogel were cut out, and then, the two pieces were brought into contact with each other in phosphate buffer (PBS, PH 7.4) solution at 25 °C for 2 min to allow them to self-heal into a complete columnar hydrogel without application of any external force. For ease of visualization, the hydrogel was dyed black and white by soaking then in PBS containing 0.002% (wt/vol) ruthenium black dye. The self-healed hydrogel supported the weight itself, and the divisions of the hydrogel

https://doi.org/10.1021/acsomega.3c04135
ACS Omega 2023, 8, 39110−39134

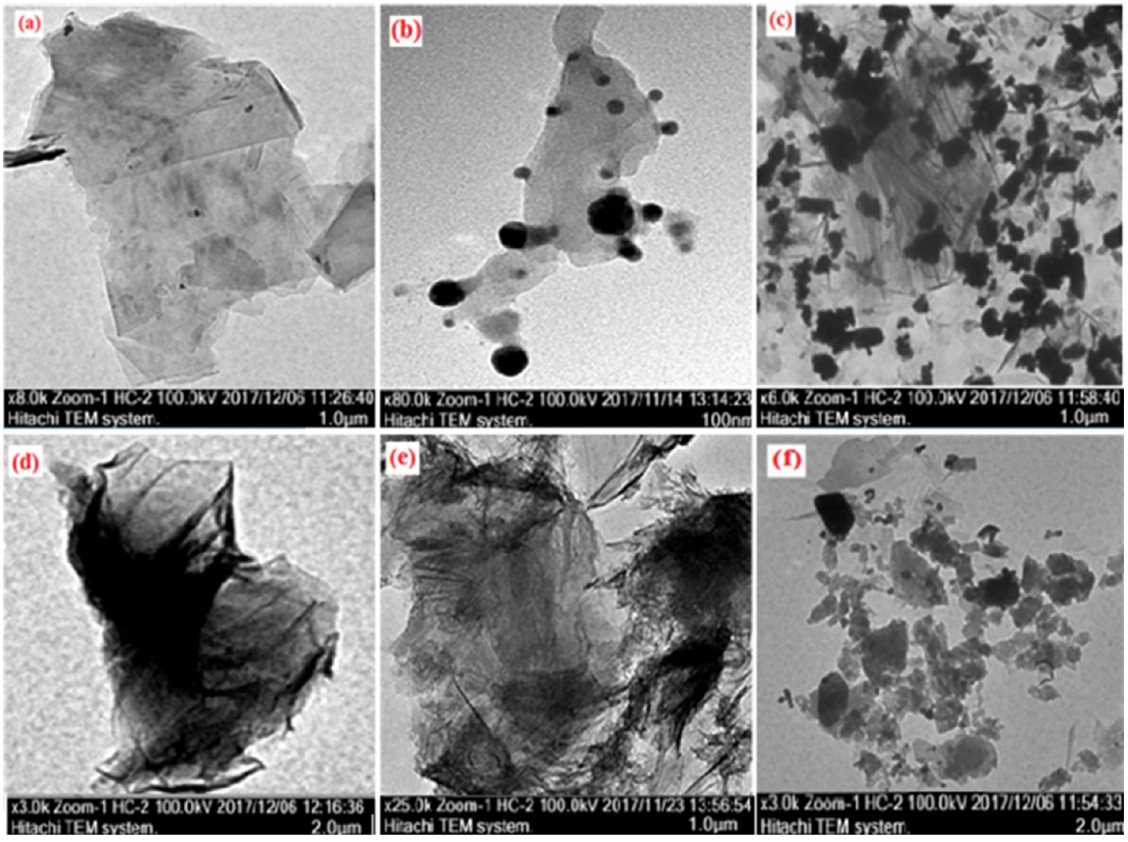

Figure 6. Representative TEM images of (a) GO, (b) GAT, (c) GATP (d) GAP-PVA, and (f) GATP-PVA.

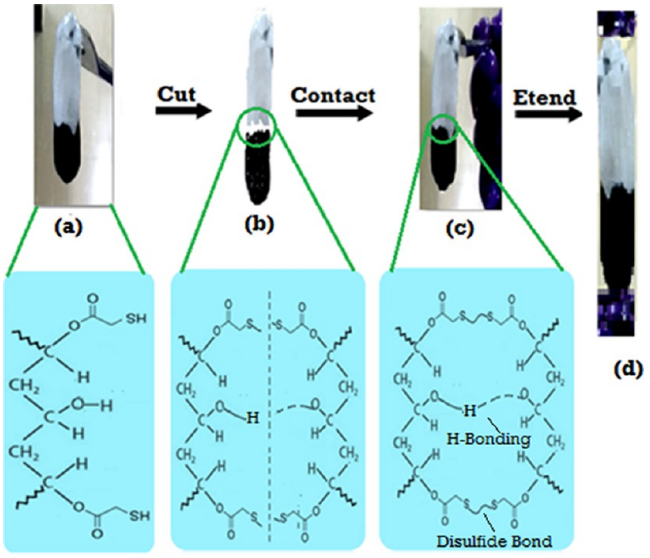

Figure 7. Images showed the self-healing capabilities of the GATP-PVA hydrogel: (a) two pieces of the original hydrogel with and without rhodamine B for coloring. (b) Two halves of the original hydrogels cut from the middle. (c) Self-healing hydrogel upon bringing the two separate halves in contact for 2 h in air at room temperature without any external stimulus and (d) extending the self-healed hydrogel to approximately 100% extension. (e) Changing step strain sweep test with less strain (γ = 1.0%) to following huge strain (γ = 500%) with 100 s for each strain interval at a constant angular frequency (10 rad/s) at 25 °C.

pieces lost their clarity. By grasping one end of the hydrogel (Figure 7d), the healed columnar hydrogel could be raised. The healed columnar remained intact when the hydrogel was bent into a U shape or stretched. All the situations of the hydrogel were photographed. The excellent and rapid self-healing properties of the hydrogel originated due to interchain linkage by H-bonding, and disulfide bonds between SH (thiol group) keep occurring in the hydrogel network ensuring their application in soft tissue regeneration and drug delivery. The recovery test of the hydrogel will be performed by the continuous step strain method, as shown in Figure 7e. After applying the first strain (500%), the G'' value of the hydrogel gradually decreases from 221 to 7 Pa, as shown in Figure 7, which indicates that the hydrogel network collapsed with others. When strain decreased up to 1%, the G'' value returned to its original value, indicating that the cross-link was partially recovered. After repeating several high-low cycle tests, the G_1'' value of the first cycle displays nearly the same value as G_2'' and G_3'' of the second and third cycles, demonstrating the self-healing behavior of the hydrogels (Figure 7).

2.9. High Tissue Adhesive Strength of the Hydrogel.

Adhesive properties of the polymer-based hydrogel are considered to be the most active for the wound because they can help stop the binding of the different tissues for proper healing. The GATP-PVA hydrogel possessed exceptional tissue adhesiveness with no skin tissue irritation or inflammatory response and adhered to the wound site completely. Figure 8A represents the properties of the prepared hydrogel, which binds to the finger of the skin six times and can be removed easily without leaving any residue on the skin. The adhesive strength of the engineered hydrogel was evaluated employing a lap shear test using bovine skins of (10 × 10 mm^2 bonding area) as the substrate and fibrin glue as the control bioadhesive. The adhesive strength of the hydrogel gradually increases from 3.4 ±

https://doi.org/10.1021/acsomega.3c04135
ACS Omega 2023, 8, 39110−39134

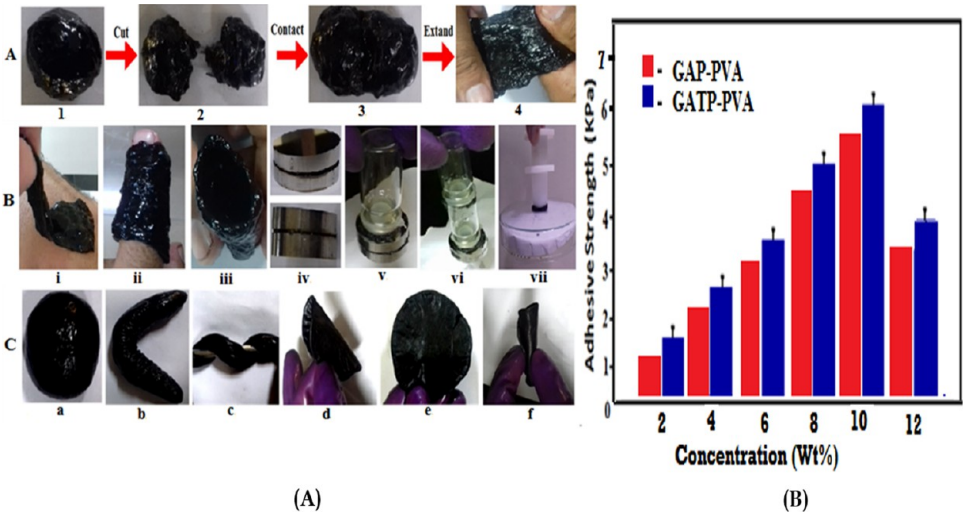

Figure 8. Tissue adhesiveness of the GAP-PVA and GATP-PVA hydrogels. (A(a)) Self-healed behavior of the hydrogel confirms the different halves connected for 2 h in air at room temperature by applying any external force (A(b)) (i) Hydrogel behavior on the author's hand. (ii) Peeling phenomena of the hydrogel adhered to the skin of the author's hand. (iii) Removal of hydrogel safely without any loss in the skin. (iv–vii) Hanging a weight box with a weight of 50 mg to 100 g. (A(c)) (a–f) Hydrogel adapts various shapes including spherical, twisting, and folding. (B) Column graph represents the effects of GAP-PVA and GATP-PVA concentrations (wt %) on the adhesion strength of hydrogel.

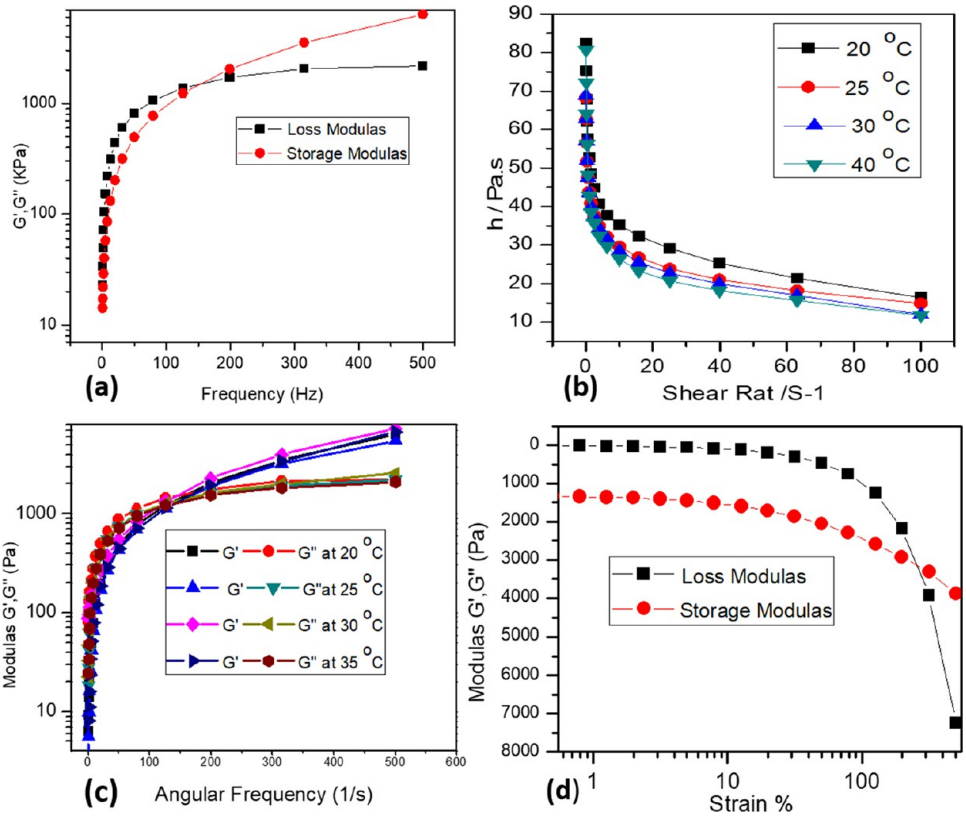

Figure 9. Rheological behavior of hydrogels (a) a graph of the storage (G') /loss modulus (G'') vs angular frequency sweep (ω) of the hydrogels at 10 rad s^{-1} at 25 °C. (b) Viscosity change of the hydrogel as a function of shear rate at different temperatures. (c) G' and G'' modulus with respect to temperature at a specific frequency (e) changing step strain sweep test with less strain (γ = 1.0%) to following huge strain (γ = 500%) with 100 s for each strain interval at a constant angular frequency (10 rad/s) at 25 °C; (d) strain amplitude sweep test (γ = 0.1–600%) at a fixed angular frequency (10 rad/s) at 25 °C.

1.2 to 6.1 ± 1.3 kPa by increasing the concentration of the engineered nanocomposites from 2 to 10% (w/v). By comparing the adhesive strength of GAP-PVA and GATP-PVA hydrogels, a remarkable difference will be noted. The GAP-PVA-based hydrogel showed 5.3 kPa adhesive property at 10% concentration as well as 6.1 kPa for the same concentration. When applied on the porcine skin, the adhesion strip cyclic test showed no loss of adhesive strength and withstood 100 g loads (Figure 8Bi). The excellent adhesive property of GATP-PVA as compared to GAP-PVA is due to the presence of sulfhydryl

https://doi.org/10.1021/acsomega.3c04135
ACS Omega 2023, 8, 39110–39134

groups (thiol group) of thioglycolic acid in GATP-PVA, resulting in Schiff base formation with primary amine of tissue protein and gelatin which increased the adhesive strength of hydrogels. As shown in Figure 8B, the adhesive strength of GATP-PVA increased with the increase in concentration and then decreased as the amount of concentration increased. This phenomenon could be ascribed to the fact that increased adhesion at the beginning might be attributed to the increased cohesion of the hydrogel in which cohesion is the restrictive factor for achieving strong adhesive strength. However, the adhesive strength might decrease as the amount of cross-linker increases due to the reduction in the reactive site for surface adhesion. The stronger adhesive strength of GATP-PVA compared with GAP-PVA might originate from the relative balance between cohesion and surface adhesion.

As shown in Figure 8B, at the initial stage, the increase of the bonding strength of the hydrogel with increasing concentration ($\leq$12 wt %) was due to the decrease of gelation time and increase in the cross-linking density between the higher content of PVA and nanocomposites. Similarly, at higher concentrations ($\geq$12 wt %), the gelation time increased and the bond strength of hydrogel gradually decreased due to the decrease of PVA content in the hydrogel, which resulted in the decrease of cross-linking properties of the hydrogel. Moreover, the higher bonding strength of GATP-PVA as compared to GAP-PVA is due to the presence of a thiol group in the GATP-PVA hydrogel which increases the intercross-linking by a disulfide bond (S−S) and H-bonding in the hydrogel matrix, as shown in Figure 8c.

Interestingly the GATP-PVA hydrogel exhibited higher adhesive strength (6.1 kPa) when compared with the fibroin glue adhesive (Greenplast) about 5 kPa, suggesting the potential adhesive property in wound healing and closure. Hence, it is not clear whether the adhesive properties are shown at the molecular level.

2.10. Rheological Characterization of Hydrogels. For the in vivo study after applying the hydrogel, skin does not show any elasticity but is also found to be rigid and tough. To know about the basic mechanism of the gelation process and rheological variations over the passage of time, one needs to modify or synthesize to improve the functional behavior of the hydrogel. Hence, it is concluded that for the better treatment of the skin, hybrid formulations were used when they were subjected to external deformation. The rheological analysis was performed at 37 °C having 10% strain (10% strain fall down in the linear viscoelastic region), and transition phenomena can be measured through G' and G'' by the function of frequency sweep and temperature, as shown in Figure 9a−e. The G' works as the indicator for the stiffness of the viscoelastic material and G'' stands for the viscous loss modulus. Figure 9a represents the early rheological behavior of the suspension at low frequency exhibiting a greater loss of G'' than the G' which confirms the viscous behavior. At higher-frequency sweep, the storage modulus (G') gradually increases and finally predominant over the loss modulus (G'') at 260% strain exhibited solid-like elastic responses ($G' > G''$). At the low frequency, G'' increased, which showed the elevated dissipation due to the reversible bond in the entire hydrogel network which showed an excellent adhesive phenomena of the hydrogel. G' at the point of intersection increases from the G'' as the frequency increases could be due to the formation of a cross-linked network. Moreover, the chain of polymer in the cross-linked network of the hydrogel does not rearrange in the short period of the time scale imposed by the deformation and stiffness to show the G' values. The point at which the storage and loss modulus curve ($G' \sim G''$) intersect (gel point) at a specific frequency sweep signals the transition from viscous behavior to solid elastic behavior and gives an estimation of the characteristic stress relaxation time in the system and provides clear evidence of the formation of viscoelastic behavior of the hydrogel. It suggested the completion of a cross-linking reaction when the G' value reached a plateau of ~1 kPa. Figure 9b shows the viscosity change of hydrogel as a function of the shear rate at different temperatures. For this study, a temperature limit of 40 °C was employed owing to the dehydration of the gel at higher temperatures. A progressive decrease in the viscosity of the hydrogel was observed from 82 to 11 Pa s with an increasing shear rate from 1 to 100 s^{-1}. It was because of the continuous break of self-assembly with increasing shearing, which led to a substantial decrease in the degree of cross-linking of the hydrogel. The change of the disrupted sol phase reversibly into the gel after shearing was also observed. The shear-thinning and thixotropic properties of the supermolecular cross-link's hydrogel are very important for biocompatible wound healing applications. The transition from sol to gel was monitored through the elastic modulus at a specific frequency with respect to the function of frequency, as shown in Figure 9c,d. The changes in G' at the temperature range 20−35 °C for all the gel were monitored, and only marginal changes in the G' values were observed. The increase of temperature at the same frequency has no effect on the elastic response of the material. It has also been confirmed that the viscoelastic modulus of the given specimen is dependent on the temperature in amplitude and not on the frequency. The recovery test of the hydrogel will be performed by the continuous step strain method. After applying the first strain (500%), the G'' value of the hydrogel gradually decreases from 221 to 7 Pa, as shown in Figure 9e, which indicates that the hydrogel network collapsed with others. When strain decreased up to 1%, the G'' value returned to its original value, indicating that the cross-link was partially recovered. After repeating several high-low cycle tests, the G_1'' value of the first cycle displays nearly the same value as G_2'' and G_3'' of the second and third cycles, demonstrating the self-healing behavior of the hydrogels. Hence, these hydrogels showed excellent mechanical properties toward the skin and avoided damage to soft tissues.

2.11. Initial Moisture Content and Swelling Behavior of the Hydrogel. The initial moisture content of the hydrogel is beneficial to accelerate the prevention of tissue dehydration during wound healing, promote angiogenesis (the growth of new blood vessels) and absorption of exude, and reduce the probability of infection. As shown in Figure 10, both the initial water content and swelling ratio of the PVA-based hydrogel decrease as the concentration of GATP increases. The swelling ratio of the hydrogel decreases from 93.5 to 72.4% as the ratio of the GATP increases from 0.1 to 1.2 wt %. A more cross-link network developed by inter- and intrapolymeric interactions, as well as a decrease in the hydrophilic group in the GATP-PVA hydrogel, which is responsible for the lower swelling volume. On the other hand, as the PVA concentration decreased in the GATP-PVA aqueous solution, the swelling ratio of the GATP-PVA hydrogel increased, but the initial moisture content of the hydrogel showed no significant changes, as shown in Figure 10. Similarly, the hydrogel with the lowest cross-linking density GATP-PVA exhibited a significantly higher amount of water uptake. Due to their higher swelling ratio and water uptake properties, the obtained hydrogel is supposed to be used for

https://doi.org/10.1021/acsomega.3c04135
ACS Omega 2023, 8, 39110−39134

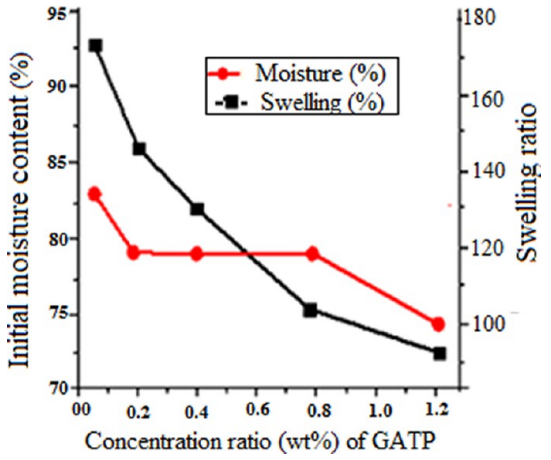

Figure 10. Initial moisture content and swelling behavior of the hydrogel.

biomedical applications, including tissue engineering, as a hemostatic agent, and drug delivery.

2.12. Rapid Gelation Time of PANI/Ag/GO/TGA/PVA (GATP-PVA) Hydrogels. The gelation time of the GATP-PVA hydrogel at room temperature showed practical biomedical applications. The effect of the feed ratio of GATP and PVA hydrogel on the gelation time was determined through the tube inversion method (Figure 11), and it has been shown that

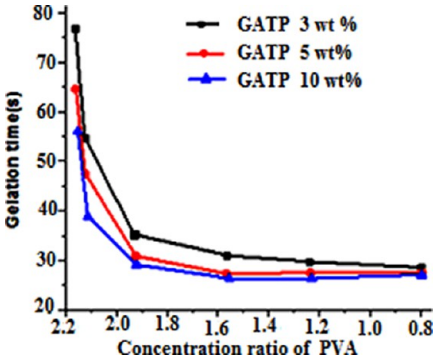

Figure 11. Amount of PVA consumed for the reactions will determine how quick GATP-PVA hydrogels are at various GATP concentrations (2.2 to 0.8 mg mL^{-1}) 3 subjects, mean ± SD.

gelation time could be adjusted by changing the concentration ratio between the GATP and PVA used for preparation. Various concentrations (3, 5, and 10 wt %) of GATP were mixed with the PVA (3%) solution having different concentrations (1:2, 1:1, 2:1, and 2:0.5). The gelation time of the two mixed solutions occurred within 30−77 s, as shown in Figure 11. When the concentration ratio of GATP-PVA decreased from 2.0 to 0.8, the gelation time reduced from 77 to 30 s, respectively. The reduction of gelation time with increasing PVA content consistently enhanced the cross-linking property of the hydrogels. At the lowest concentration of PVA, the influence of GATP on the gelation time was remarkable, and at higher concentrations, it was not prominent. The gelation process and viscoelastic properties of the hydrogel were investigated by monitoring the variation of the storage modulus (G') and loss modulus (G'') as a function of time during the cross-linking process. As shown in Figure 7a,b, G' is elevated rapidly in the initial stage when compared to G'' due to the gradual formation of the elastic hydrogel that resulted from the cross-linking network of different residues. The point at which the storage modulus (G') and loss modulus (G'') curve intersect (gel point at ∼1 kPpa) at the specific time provided gives clear evidence of the formation of viscoelastic behavior (gel formation) of the hydrogel. Due to the intimate relation between the hydrogels and the wounds in the system, the GATP-PVA (10%) ratio of 2.1 showed a gelation duration of 56 s which is considerable for wound treatments.

2.13. Electrochemical Characterization and Conductivity of Hydrogels. To evaluate the electroactivity of the hydrogel was conducted in four experiments, including the reversible doping/de-doping test, UV−vis spectra of stepwise oxidation from LM to EM state, cyclic voltammetry (CV), and four-probe test. First, the doping/de-doping test was carried out by immersing the hydrogel in 1 M HCl/NaOH solution, and repeatedly, a change in color from electroactive form EMs (green) to insulative form LM (blue) was observed, confirming that the hydrogel has the reversible doping/dedoping ability, as shown in Figure 12A. The UV spectra exhibited a stepwise oxidation process from the LM to the EM state. It was found that the LM state of the hydrogel showed two absorption peaks at around 450 and 620 nm (Figure 12B) attributed to the $\pi-\pi^*$ transition of the benzenoid ring and the n-π^* excitonic transition of the benzenoid to the quinoide ring in the emeraldine base PANI backbone structure, respectively. After doping with 1 M HCl, the hydrogel showed a slight blue shift of the benzenoid absorption peak to about 420 due to the formation of delocalized polarons, which was attributed to the generation of emeraldine salts (EMs) and electroactivity of the hydrogel to conduct electrons in the polymer chain. The electroactivity of the hydrogel in 1 M HCl was further studied by cyclic voltammetry, as shown in Figure 12C. The CV curves for all samples clearly indicate that the redox reaction progresses in the electrodes. The arrows indicate the scan direction. All the samples show reversible reduction and oxidation in the 1 M HCl electrolyte. These redox/oxid properties of the hydrogel such as the emeraldine oxidation state changed to the pernigraniline/leucoemeraldine state. The higher current density of the electroactive hydrogel can be attributed to its higher electrical conductivity, fast ion transport, and high surface area. Finally, the conductivity of the hydrogel in 1 M HCl was further determined by the four-point probe method, and the result is presented in Figure 12D. Both types of hydrogel showed conductivities of 4.25 and 3.82 mS/cm at 37 °C which was attributed to the amine and carboxyl groups in the polymer chain of the hydrogel. Interestingly, the ionic conductivity of the GATP-PVA hydrogel was most related to the human muscle and skin (4.1 mS/cm), dermis (2.2 mS/cm), and epidermis (0.26 mS/cm) of the skin. Although the electrical conductivity in vivo is quite low, conductivities play an important role in chemical ion exchange and signal transforming between the cells in life activities. All these results suggest that as-prepared hydrogels have adjustable electroactivity which would be helpful for sending electrical signals in the form of impulses from biological tissue that is still alive and promote wound healing.

2.14. Tensile Properties of GAP-PVA and GATP-PVA-Based Hydrogels. The typical stress−strain curves obtained from the tensile measurement of pure PVA and PVA-based hydrogels (GAP-PVA and GATP-PVA) with different ratios of PVA to GATP nanocomposite are presented in Figure 13a. It is clearly shown that at the beginning, the breaking strength displayed the trend of first increasing and then decreasing with

https://doi.org/10.1021/acsomega.3c04135
ACS Omega 2023, 8, 39110−39134

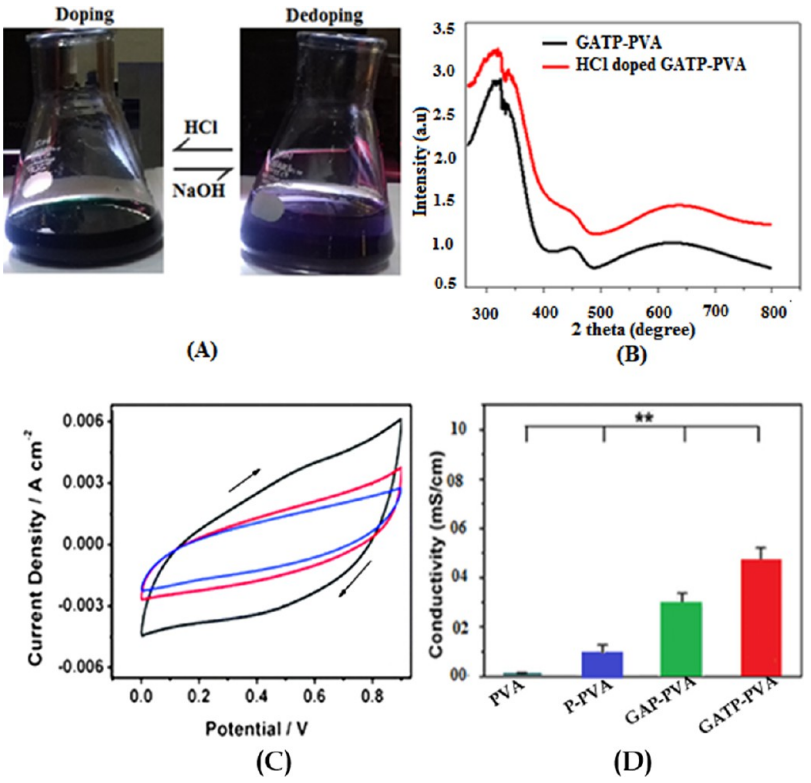

Figure 12. Electrochemical characterizations of (A) reversible doping behavior of hydrogels by repeatedly alternately immersing the hydrogel in I mole HCl and NaOH solution. (B) UV−vis spectra of hydrogel aqueous solution in the LM state and EMs in water and doped with 1 M HCl aqueous solution. (C) Cyclic voltammogram of the GATP-PVA hydrogel in 1 mol^{-1} HCl solution with a scan rate of 10 mV/s and Hg/Hg_2Cl_2 as a reference electrode. (D) Conductivity of the GATP-PVA and GAP-PVA hydrogels (Four point probe method). Scale bar: 100. *$P < 0.05$.

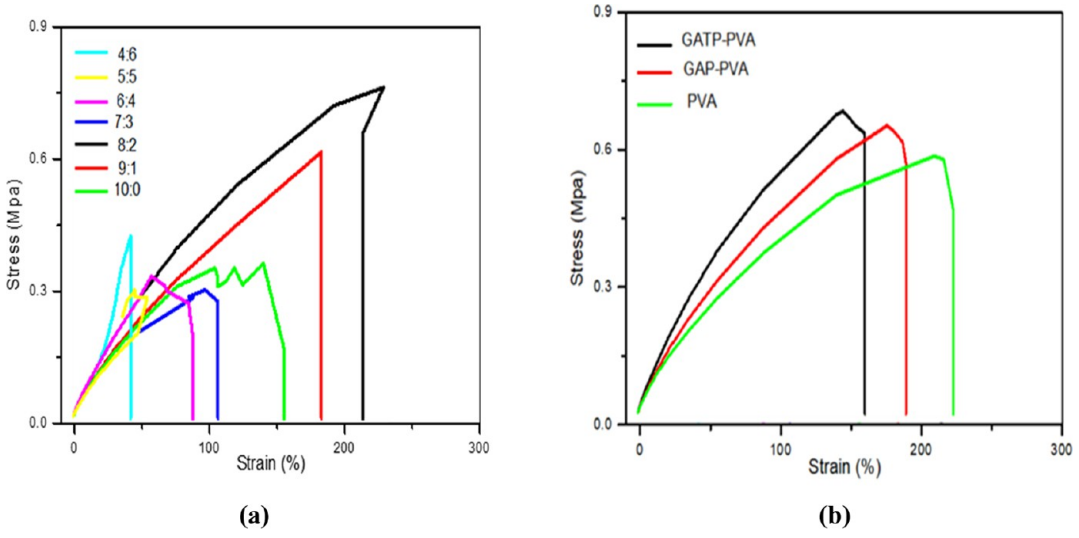

Figure 13. Tensile strength behavior of the synthesized hydrogel.

the increasing of PVA content. The PVA−GATP ratio of 8:2 displays the highest breaking stress (0.786 MPa) and the breaking strain (286%) compared to other hydrogels. The higher stress and strain of the specified hydrogel are due to good dispersion of the nanocomposite in the PVA matrix which promotes a higher cross-linking network between the cation of the composite material and PVA of the hydrogels. As reported in several previous studies, the PVA hydrogel owned the main drawback of weak strength; hence, the tensile strength of the PVA-based hydrogel (GATP-PVA) increases with the increase in the concentration of PVA content. When the PVA-based hydrogel is stretched, dispersed particles are destroyed, and the secondary nanoparticle scatters in the PVA matrix and reforms the dynamic fracture, so confined intermolecular H-bonds promote the chain extension and alignment upon stretching in GATP-PVA hydrogels. Through the strain-induced scattering and enmeshment effect of GATP on the PVA hydrogel via strong intermolecular sacrificial H-bonds, the external load energy can be efficiently dissipated and the stress concentration is then gradually retarded; thus, eventually, reinforcing the

https://doi.org/10.1021/acsomega.3c04135
ACS Omega 2023, 8, 39110−39134

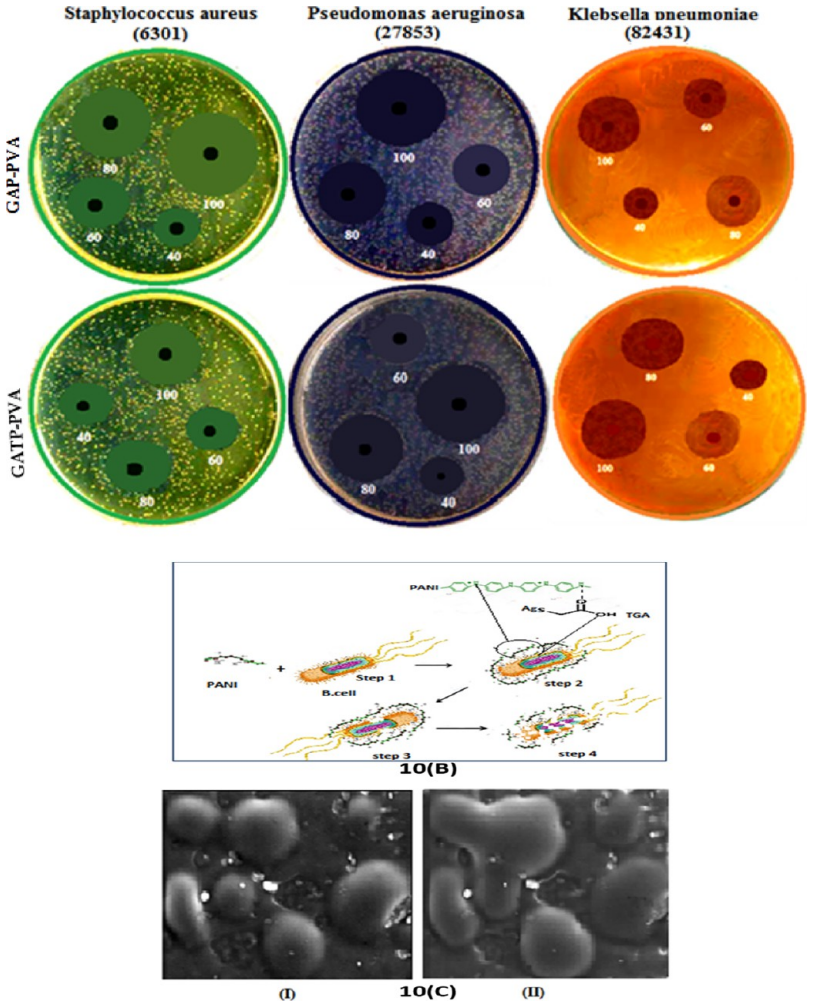

Figure 14. (A) Antibacterial activity of the prepared GAP-PVA and GATP-PVA hydrogel against multi-drug resistance pathogens *Klebsiella pneumoniae* (82431), *Pseudomonas aeruginosa* (27853), and *Staphylococcus aureus* (6301) using different concentrations of nanocomposites (40, 60, 80, and 100 μg/mL). **10** (B) Antibacterial activity mechanism of the GATP-PVA hydrogel. **10** (C) SEM images showing cell membrane damage of *S. aureus* C (I) control C(II) treated.

strength, toughness, and the initiation of microcracks is postponed. In order to compare the mechanical properties of GATP-PVA and GAP-PVA with pure PVA, a series of tensile tests were carried out, and the results are displayed in Figure 13b. The GATP-PVA shows the highest breaking stress (0.72 MPa) as compared to GAP-PVA (0.6 MPa). The higher tensile strength of the GATP-PVA as compared to GAP-PVA is due to a higher cross-link network of the thiol group with the PVA matrix and thus restricted the polymer motion and decrease in the elongation at break in the GATP-PVA hydrogel.

3. ANTIBACTERIAL ACTIVITY OF THE WOUND DRESSING

Bacteria are the main cause of wound infection; therefore, the antibacterial activity of the electroactive hydrogel-based dressing should be evaluated before it is put in for wound healing applications. To evaluate the antibacterial activity, a zone of inhibition test (agar disc-diffusion method) along with MIC and MBC was carried out against multidrug resistance *Staphylococcus aureus* MDR (6301), *Pseudomonas aeruginosa* (27853), and *Klebsiella pneumoniae* MDR (82431). The zone of inhibition of various strains of bacteria with different concentrations of hydrogel (40, 60, 80, and 100 μg/mL) is shown (Figure 14).

The result given in Table 2 indicates that both types of hydrogel (GATP-PVA, GAP-PVA) exhibited strong antibacterial potential against the tested strains of pathogens. The maximum zone of inhibition shown by the GATP-PVA hydrogel against *Staphylococcus aureus* MDR (6301) was (25.83 $\pm$ 0.72) alongside MDR *Pseudomonas aeruginosa* (27853) with an inhibition zone of 22.73 $\pm$ 0.41. *Klebsiella pneumoniae* (82431) exhibited a minimum inhibition zone of 21.66 $\pm$ 1.15 in this investigation. The GAP-PVA hydrogel also showed a maximum zone of inhibition 21.51 $\pm$ 0.35 against *Staphylococcus aureus* MDR (6301) and a minimum zone of inhibition (17.13 $\pm$ 0.21) against *Klebsiella pneumoniae* (82431). Minimum MIC (10) μg/mL values for the MDR isolates included in this investigation were recorded for *Klebsiella pneumoniae* (82431) and MDR *Pseudomonas aeruginosa* (27853), as shown in Table 2. Generally, MIC and MBC ranged between 10−20 and 2.5−10 μg/mL, respectively (Table 2).

The less variation in the zone of inhibition showed that the structural and chemical changes of Gram-positive and Gram-negative bacterial cell surfaces play a major role in the antibacterial activity. Although the exact mechanism of the bactericidal action of the electroactive hydrogel is yet not fully

https://doi.org/10.1021/acsomega.3c04135
ACS Omega 2023, 8, 39110−39134

Table 2. Antimicrobial Activities of GAP-PVA and GATP-PVA-Based Hydrogels at Different Concentrations against Different Clinical Bacterial Isolates

	concentration of synthesized hydrogel and zone of inhibition (mm)									
	GAP-PVA			GATP-PVA			Cefixime			
strain	40 (μg/mL)	60 (μg/mL)	80 (μg/mL)	100 (μg/mL)	40 (μg/mL)	60 (μg/mL)	80 (μg/mL)	100 (μg/mL)	40 (μg/mL)	60 (μg/mL)	80 (μg/mL)	100 (μg/mL)
S. aureus MDR (6301)	12.16 ± 1.25	15.83 ± 0.28	17.16 ± 0.76	18.66 ± 0.28	15.1 ± 2.0	18.16 ± 1.04	19.5 ± 0.5	21.16 ± 1.04	18.16 ± 1.25	21.2 ± 0.2	21.3 ± 0.1	25.83 ± 0.76
P. aeruginosa MDR (27853)	14.5 ± 1.32	17.16 ± 1.04	19.5 ± 0.5	21.83 ± 0.57	13.66 ± 0.28	16.5 ± 1.5	18.83 ± 1.25	20.33 ± 1.25	16.66 ± 0.28	17.16 ± 0.76	21.5 ± 0.5	23.83 ± 1.04
K. pneumoniae MDR (82431)	13.1 ± 2.02	15.33 ± 1.44	17.16 ± 1.04	19.66 ± 0.28	16.66 ± 1.52	18.16 ± 0.76	21.66 ± 0.28	23.66 ± 0.57	15.33 ± 1.44	17.6 ± 0.86	19.83 ± 0.76	24.66 ± 0.28

All of the results are displayed in systematic triplicates ($p \leq 0.05$).

understood, the most common proposed mechanism of toxic action is illustrated in Figure 14B).

Step (1). In the first step, imino sites of the PANI matrix and the carboxylate group of thioglycolic acid bind to the polysaccharide chain of the bacterial cell wall through electrostatic interactions.

Step (2). Due to this attachment, the change in the potential gradient arises on the ion channels present on the cell wall of bacteria, as a result of which the normal influx and efflux of ions are disturbed.

Step (3). PANI nanocomposites release the dopant ions on the attachment sites that change the PH of the bacterial cell, and the permeability of the ion is disturbed on the bacteria cell wall.

Step (4). The dopant ions penetrate the semipermeable membrane of B. cell followed by the disruption of ATP production, protein synthesis, as well as DNA replication and alter the cell composition leading to cell lysis. Therefore, wound healing can be accelerated by the enhanced synergistic effect of multifunctional materials to kill bacterial pathogens. The change in the morphology of bacteria cells treated with the electroactive hydrogel was examined by SEM, as shown in Figure 14C. The SEM image reveals that the controlled and not treated were blunt round ends and smooth surfaces (Figure 14CI). After treatment with the conductive hydrogel, the morphology of the bacterial cell was irregular, and some of the surfaces were dented, wrinkled/broken (Figure 14CII). Therefore, wound healing can be accelerated by the enhanced synergistic effect of the multifunctional materials to kill bacterial pathogens, although it is shown to be joined to oxidative phosphorylation and disturbance of the electron transport and changing its permeability at the B-cell membrane due to high electrostatic charge on the surface of PANI and the presence of the amino-thiol group. The antibacterial activities of the hydrogel were compared with the standard drug Cefixime which demonstrates that both hydrogels exhibited excellent bactericidal activity against the MDR bacterial isolate. The scatter plot of the inhibition zone versus concentrations of nanocomposites against different strains of bacteria is presented in Figure 15a–d, with overall experimental result depiction for the development of new antimicrobial wound dressing with efficient protection against different pathogen infections (Table 3).

4. ANTIOXIDANT ACTIVITY AND FREE RADICAL SCAVENGING EFFECT

Production of reactive oxygen species (ROS) under oxidative stress by polymorphonuclear neutrophils (PMNs) at the site of tissue injury plays a central role in the progression of many inflammatory disorders because they oxidize protein and damage the DNA and lipid cellular constituents. The antioxidant hydrogel could reduce oxidative damage by reacting with free radical species and removing O_2 in the process of ROS extracellular transmission. The concentration of the hydrogel is important for radical scavenging (Figure 16a). Both types of hydrogel (GAP-PVA, GATP-PVA) showed considerable radical scavenging having an IC_{50} value of 115.2 ± 1.43 and 113.0 ± 3.70 μg/mL by reducing the DPPH free radical to a yellow-colored compound (diphenylpicryhydrazine). Ascorbic acid was found to be the best one for radical scavenging assay with an IC_{50} value of 18.12 ± 0.90 μg/mL as compared to GAP-PVA and GATP-PVA, respectively. The absorption peak of DPPH at 517 nm progressively disappeared with poss of time interval (5 min to 3 h) for the neutralization and hydrogen to scavenge the

https://doi.org/10.1021/acsomega.3c04135
ACS Omega 2023, 8, 39110−39134

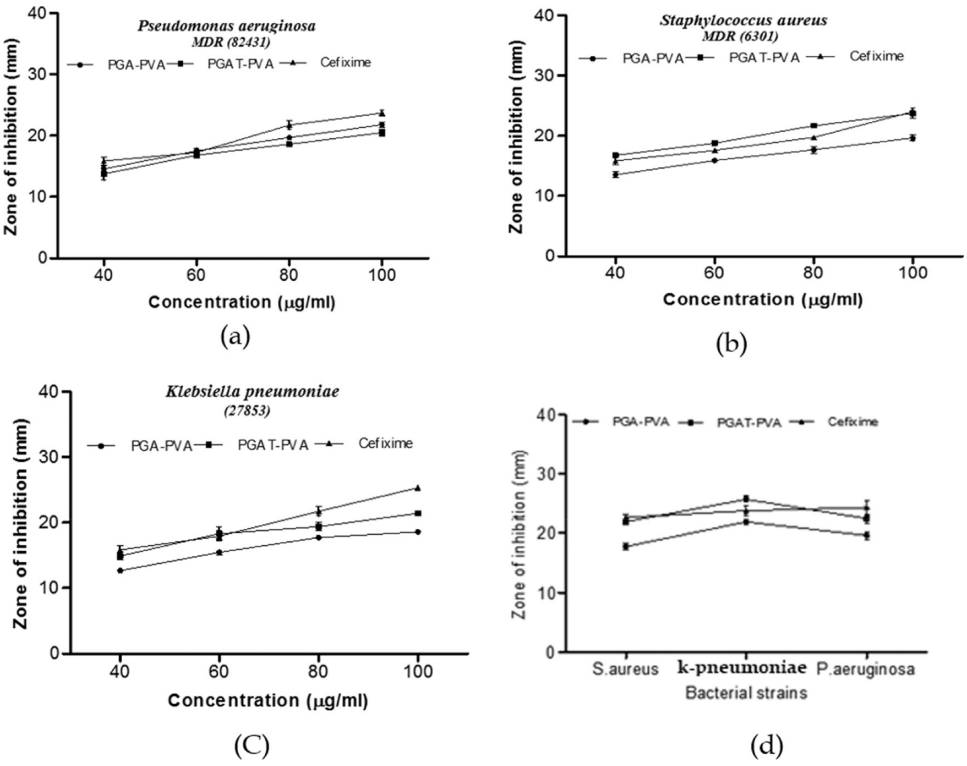

Figure 15. Combined antibacterial trial of GAP-PVA and GATP-PVA against multi-drug resistance pathogens (a) *Pseudomonas aeruginosa* (27853), (b) *Staphylococcus aureus* (6301), (c) *Klebsiella pneumoniae* (82431), using different concentrations of nanocomposites (40, 60, 80, and 100 μg/mL), and (d) comparative study of GAP-PVA and GATP-PVA against all the three types of multidrug resistance bacteria (*S. aureus* (6301), *P. aeruginosa* (27853), and *K. pneumonia* (82431).

Table 3. Antimicrobial Activity of Hydrogels against Different Multidrug Resistant (MDR) Bacteria[a]

	GAPP (100 μg/disc)				GATPP (100 μg/disc)				Cefixime (100 μg/disc)			
strains	zone of inhibition (mm)	MIC	MBC	MBC/MIC	zone of inhibition (mm)	MIC	MBC	MBC/MIC	zone of inhibition (mm)	MIC	MBC	MBC/MIC
S. aureus MDR (6301)	21.51 ± 0.35	20	05	04	25.83 ± 0.72	20	10	02	22.83 ± 0.76	10	05	02
P. aeruginosa MDR (853)	19.63 ± 0.31	10	2.5	04	22.73 ± 0.41	20	05	04	24.66 ± 1.25	20	05	04
K. pneumoniae MDR (82431)	17.13 ± 0.21	20	10	02	21.66 ± 1.15	10	2.5	04	22.66 ± 1.15	10	1.25	08

[a]Note* MIC, minimum inhibitory concentration; MBC, minimum bactericidal concentration; MB/MIC (ratio).

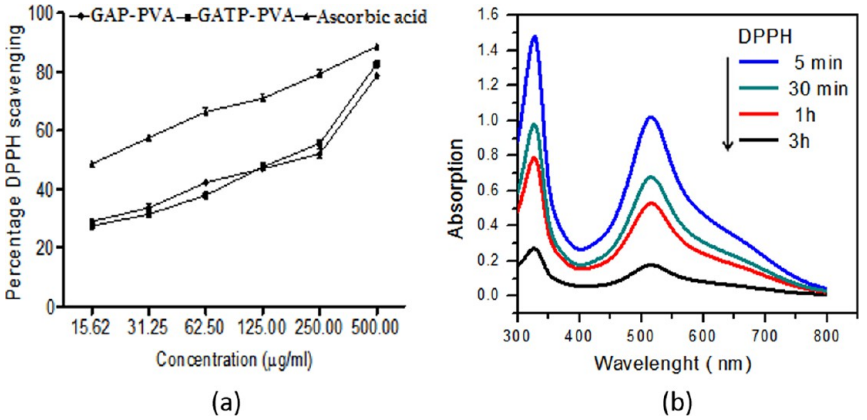

Figure 16. Antioxidant activity of the hydrogel. (a) DPPH scavenging percentage by the GATP-PVA hydrogel with different concentrations. (b) UV–vis spectra of the DPPH+ GATP-PVA hydrogel at different intervals of time.

DPPH free radicals with increasing time and change the molar ratio of GATP-PVA and DPPH, as shown in Figure 16b.

The DPPH scavenging activities of the test sample exhibit the quantity of antioxidants found in the reaction mixture, and there

https://doi.org/10.1021/acsomega.3c04135
ACS Omega 2023, 8, 39110−39134

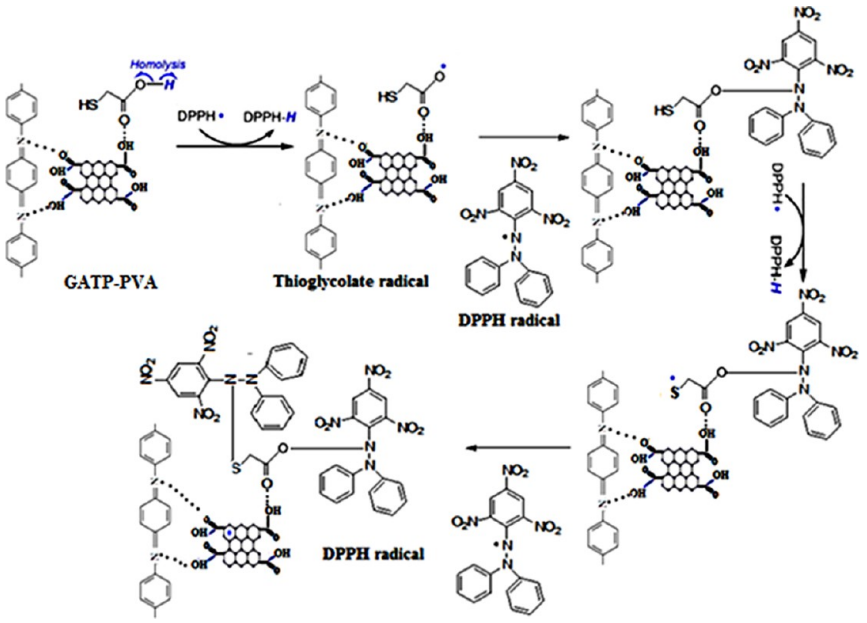

Figure 17. Mechanism reaction between thiol-functionalized graphene oxide with polyaniline and DPPH.

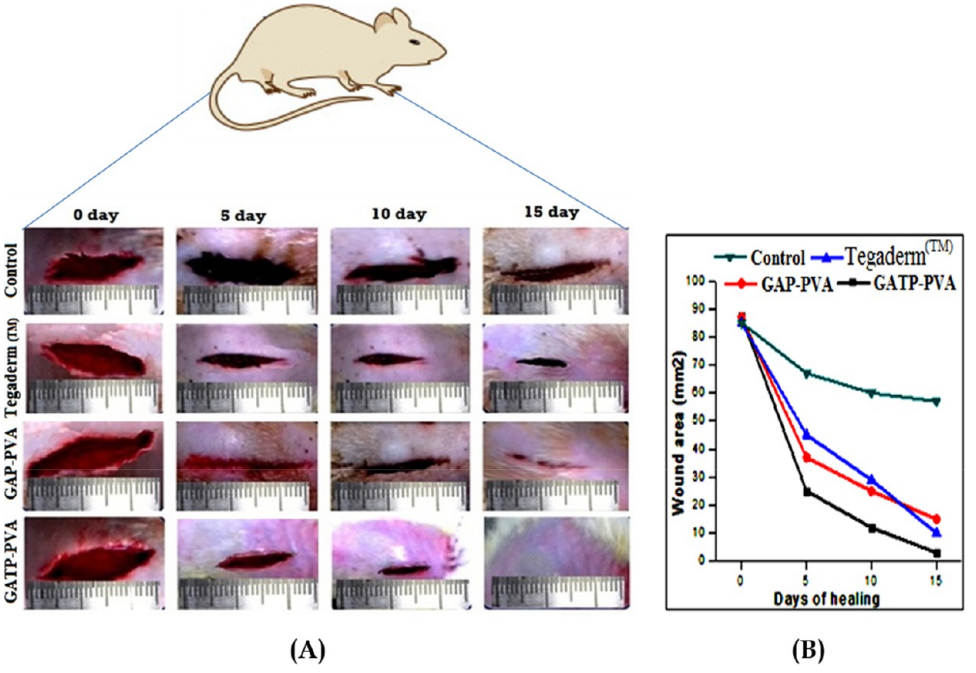

Figure 18. (A) With the help of photographs, morphometric characters of the wound are observed at 0th, 5th, 10th, and 15th for different treatment groups in rats. (B) Wound contraction graph with respect to healing days of the entire group.

is virtually a linear small change. This is due to the fact that greater hydrogen atoms can be donated for the elimination of more DPPH samples that are present. In comparison to GAP-PVA, GATP-PVA showed a higher DPPH scavenging efficiency for a given amount of material. The increase in the surface area, availability of reaction sites on the thiol group, and higher number of hydrogen atom donors for a given weight of the sample are thought to be due to this phenomenon.

The evolution of a material's antioxidant activity over time showed that up to a certain point, the rate of DPPH scavenging activity moves smoothly. Afterward, the rate of DPPH scavenging activity declines. This shows that the partially amine- and partially imine-containing polyaniline in EMS was converted into the fully oxidized form of the permigraniline state by donating one hydrogen atom to the DPPH free radical, which caused the peak intensity at 517 nm to decrease until it was unable to contain any hydrogen atoms for reducing DPPH. The absorption band of DPPH at 517 nm reveals that the antioxidant activity of nanocomposites depends on the ability to dedicate hydrogen to scavenge the DPHH free radicals (Figure 17).

The mechanism of the reaction between thiol-functionalized graphene oxide with polyaniline and DPPH shows that the antioxidant property of the sample increases with the increase in the proportion of thiol block. This can be attributed to the fact that the thiol group owing to its redox-active nature is efficient in scavenging DPPH and the antioxidant activity of the material.

https://doi.org/10.1021/acsomega.3c04135
ACS Omega 2023, 8, 39110−39134

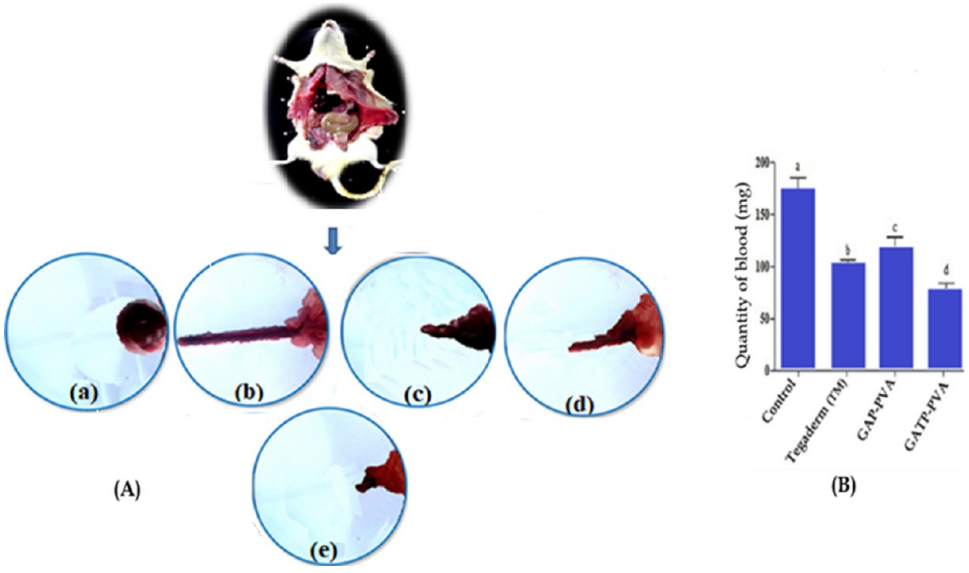

Figure 19. Evaluation of the hemostatic ability of the hydrogel: (A) (a) preparatory phase, (b) hemostatic activity of the DMSO-treated group (control blood), (c) Tegaderm-treated group, (d) GAP-PVA-treated group, and (e) GATP-PVA-hydrogel-treated group; (B) total loss of blood from the pricked rat liver after 3 min (mean ± SD, $n = 3$), showing significant level $p < 0.05$.

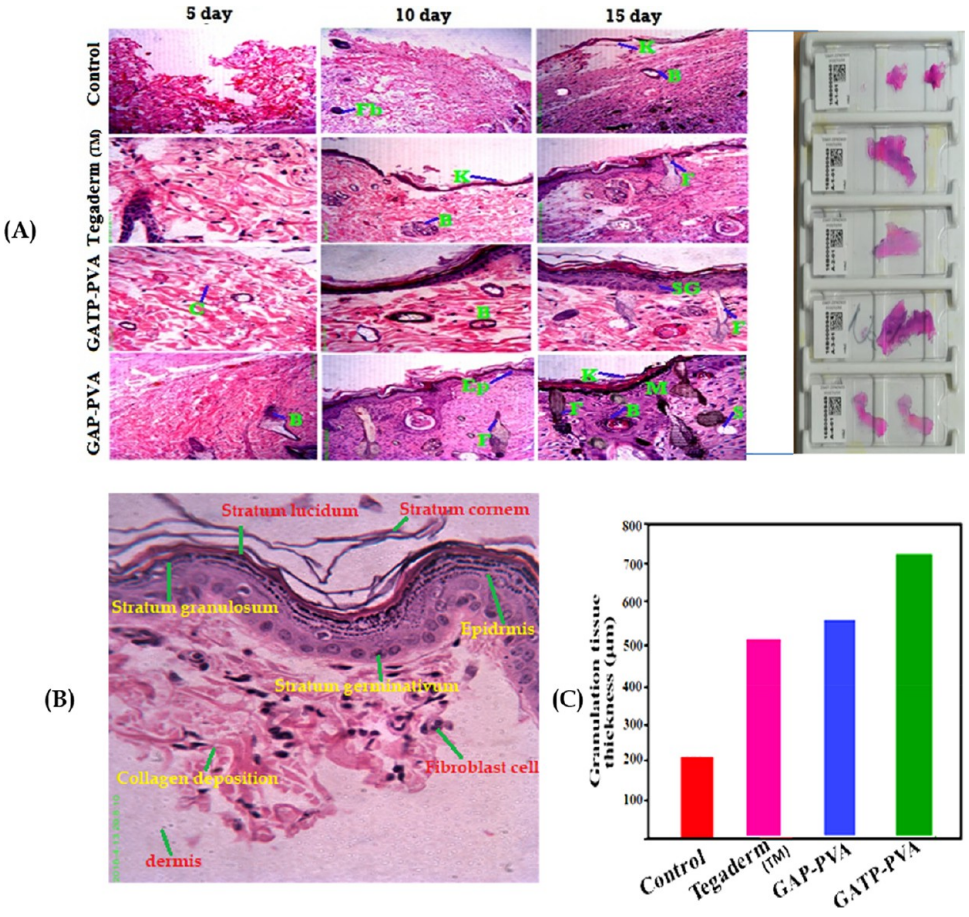

Figure 20. (A) H&E-stained histological section (granulation tissue, magnification 40×) of rat skin at various time intervals (Days 5, 10, and 15) during wound healing, control (DMSO-treated group), Tegaderm-treated group, GAP-PVA-treated group, and GATP-PVA-treated group. (B) High magnified histological section (80×) of the GATP-PVA-treated rat skin after 15 days. (C) Graphical representation of the granulation tissue thickness for the control group, Tegaderm group, hydrogel GAP-PVA, and hydrogel GATP-PVA on the 15th day, scale bar 200 mm (showing significant level $P < 0.05$). Abbreviation: Fb, fibroblast cell; F, hair follicle; S, sebaceous glands; K, keratinized layer; Ep, epidermal layer; B, blood vessels; C, collagen deposition; SG, Stratum granulosum; M, melanocytes.

https://doi.org/10.1021/acsomega.3c04135
ACS Omega 2023, 8, 39110−39134

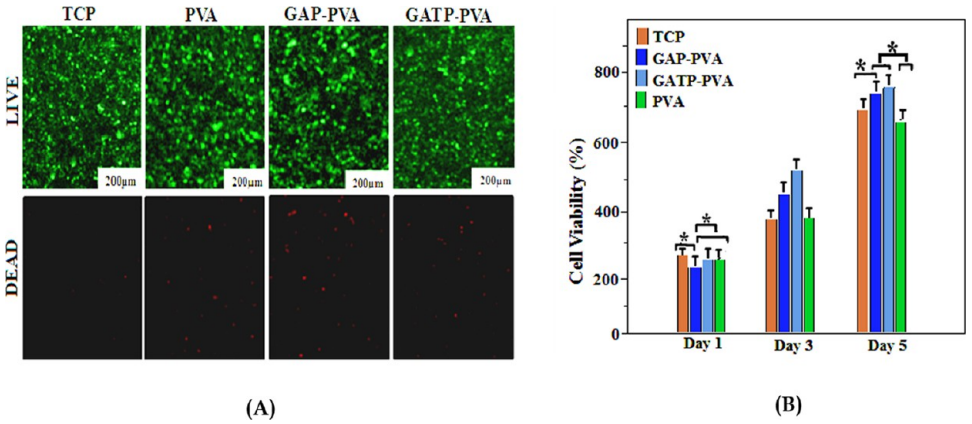

Figure 21. (A) Fluorescence Live/dead staining of L929 cells on the 5th day for, PVA, GAP-PVA, GATP-PVA, and TCP. Scale bar 250 μm. (B) Cell viability evaluation of hydrogels by contacting with the L929 fibroblasts cultured for 5 days, $^*P < 0.05$. Note: Live and dead images were taken from the exact same spot on the hydrogel surface and at the same magnification.

5. IN VIVO STUDY FOR THE EFFECTS OF THE DRESSINGS ON INCISION WOUNDS

Wound healing is an intricate process of cellular interaction that leads to resurfacing and restoration of the tensile strength of injured tissue. This process is depicted in a discrete phase including hemostasis, granulation, and maturation. The wound contraction rates of different groups on different days (0, 5, 10, and 15) are presented in Figure 18A. Wound contraction was noted to be 15, 35, and 55% for the negative control group whereas 30, 50, and 65% for the positive control at days 5, 10, and 15 respectively. A hydrogel-treated group exhibited the highest wound contraction percentage (35, 55, and 85% for the GAP-PVA hydrogel group and 40, 65, and 90% for the GATP-PVA hydrogel group) on respective days. The negative control group exhibited scab formation which stuck on the wound area, and low bleeding was observed while inflammation was noted on its removal even after 15 days. The excellent wound healing effect of the GATP-PVA hydrogel as compared to the control group could be attributed to the synergistic antibacterial properties, scavenging free radical ability, higher electrical conductivity, and porous structure which avoided excessive inflammation, accelerated re-epithelialization, and benefited from maintenance of the wound current and acceleration of wound.

5.1. Hemostatic Properties of the Hydrogel. The hemostatic or blood clotting agent is an important material that helps prevent excessive bleeding when a blood vessel is injured or in case of surgery. To further investigate the practical application of the electroactive hydrogel as a hemostatic material in vivo using a hemorrhaging liver mouse model. The quantitative result of the total blood loss at the preparative phase, control group, Tegadern-treated, and rats treated with hydrogels (GAP-PVA, GATP-PVA) on the hemorrhaging site of the liver pricked with a needle was determined on the filter paper (Figure 15A). The overall blood loss from the groups after 3 min was 176.65 ± 12.90 mg, markedly reduced ($p < 0.05$) blood loss to 102.33 ± 5.75 and 118 ± 10.59 mg corresponding to Tegaderm and GAP-PVA hydrogels, whereas rats treated with GATP-PVA hydrogel significantly ($p < 0.05$) decreased the blood loss (76.58 ± 6.03 mg), as shown in Figure 19B. This result demonstrates that both hydrogels (GAP-PVA, GATP-PVA) exhibit excellent hemostatic activity and have remarkably reduced the loss of blood and bleeding time of the liver. The excellent hemostatic activity of hydrogel was due to good adhesive properties onto the surrounding tissue, rapid gelignite, and self-governing healing ability, which allow the formation of fibroblasts through the chemo-static effect and enhance collagen formation.

5.2. Histopathological Study of the Regenerated Tissues. Histopathological studies are normally used to evaluate and observe the efficiency of different dressings on the wound healing process including re-epithelization, fibroblast immigration, collagen production, and infiltration of inflammatory cells, as shown in Figure 20. Histopathological studies of wound regenerations in different phases within 15 days were conducted by H&E staining. The H&E-stained section of the Tegaderm-treated group and hydrogel GAP-PVA group on the fifth day displayed enhanced inflammatory cell infiltration, reticular collagens fibrous with a few fibroblast cells, and thin epithelization layer of epidermis cells. Interestingly, hydrogel GATP-PVA group tissues exhibited denser collagen layers, new blood vessels, better reepithelization process, and connective tissue with more fibroblast cells and prickle cells, as compared with the Tegaderm-treated group and the GAP-PVA hydrogel group. On the 10th day, the hydrogel GATP-PVA treated group displayed higher regularity in both epithelium and connective tissue with more fibroblasts, abundant collagen, keratinocytes, hair follicles extend to horny layer of epithelial cell with sebaceous gland and new blood vessel than the two control groups. At 15 days, wounds in the Tegaderm-treated group and hydrogel GAP-PVA exhibited collagen fibrous with the reticular arrangement, few hair follicles with the sebaceous gland, thin basement membrane, little prickle cell, and stratum granulosum along with the blood vessel. The hydrogel GATP-PVA-treated group displayed more ordered and parallel collagen fibers with no inflammatory cells, stratum granulation with large basement membranes, melanocytes cells, large hair follicles, and thick layers of epidermis cells as compared to the positive and negative control groups after 15 days. Untreated rats displayed incomplete healing in wound tissue with immature granulation, acute inflammatory cells, blocked blood vessels, disfigured collagen deposition, and less epithelization in histopathological studies even after 15 days. The in vivo study indicates that the excellent wound healing ability of hydrogel GATP-PVA is due to multifunctional properties (such as electroactivity, good antibactericidal and scavenging free radical activity, porous nature, and flexibility), which affect the fibroblast cell migration

https://doi.org/10.1021/acsomega.3c04135
ACS Omega 2023, 8, 39110−39134

and proliferation of tissue, thus promoting the wound healing process.

5.3. In Vitro Cytocompatibility Assessment of Hydrogels (Cell Viability). Favorable cell compatibility is essential for designing new wound dressing materials. Therefore, the cytotoxicity of the hydrogel (GATP-PVA and GAP-PVA) having various concentrations (25, 50, and 100 μg/mL) was evaluated by the direct contact test between the L929 fibroblast cell line and hydrogel. A conventional LIVE/DEAD cell viability assay was used for this purpose and results are given in Figure 21A. None of the cytotoxicity records for the hydrogel because cell viability was found to be more than 95% (Figure 21A). Although no significant difference ($P \geq 0.05$) between the cell viability on different samples after the first day postseeding. After the first day of cell culture, the viability of cells cultured with neat PVA (92.2 ± 3), GAP-PVA (94.4 ± 2.3), GATP-PVA (95.8 ± 1.2), and hydrogels were close to each other. The number of adherent and proliferating cells on electroactive samples furthermore considerably increased with the addition of 3 and 5 days to the culture time (GAP-PVA, GATP-PVA) ($P < 0.05$) was detected in comparison to the TCP nonelectroactive group (Figure 20A). In addition to supporting the result of the cell viability assay, we further evaluated the effect of different concentrations of the hydrogel (25, 50, and 100 μg/mL) on the proliferation of the cell line. None of the cytotoxicity records for both hydrogels because cell viability was found to be more than 95%. No significant difference ($P \geq 0.05$) between the cell viability on different hydrogels with different concentrations was observed, and the viability of cells was very close to each other. An increase in the culture time was observed after 120 h (5 days).

The cell proliferation rate of GATP-PVA and GAP-PVA ($P < 0.05$) increases as compared to TCP and PVA. The lower viability found at 24 h (1 day) compared to values obtained upon 120 h (5 days) of incubation could be related to the interaction of electroactive hydrogel (GAP-PVA and GATP-PVA) with the cells. Afterward, the residual viable cells started to multiply, and consequently, the viability was raised. This phenomenon was linked to the presence of electroactive moieties in the hydrogel network which transmitted electro-signals to adherent cells through their distinct electro-conductive nature and induced the exchange of chemicals and energy between the cells improving fibroblast cell growth and proliferation. Previous research has shown the impact of charge moieties on the protein adsorption process and the growth of adherent cells; however, at excessive concentrations, toxicity may occur. The morphology of adherent cells on a hydrogel surface did not differ morphologically from that of TCP which showed that cells cultivated on a hydrogel preserve their typical morphologies and spreading. In addition, the LIVE/DEAD test makes it clear (Figure 20A) that the intensity of green (live cells) fluorescence is very high and a lot of cells can be seen on the hydrogel surface (GAP-PVA, GATP-PVA) and TCP, while in the same region of the hydrogel, there are few to none red (dead cell) fluorescence sports appeared in all groups due to normal cellular metabolism and apoptosis. It has to be noted that focusing on the whole region of the hydrogel surface at this magnification is very difficult because hydrogel inevitably exhibits some folding and wrinkles in the medium. Both the LIVE/DEAD staining and cell proliferation results exposed that both types of electro-conductive hydrogels had better cytocompatibility than TCP and they could be promising candidates as novel wound dressing materials with the ability to encourage faster tissue recovery.

5.4. Hydroxyproline Content in the Wounds. Hydroxyproline is a major component of the protein collagen that serves as a biochemical marker in reference to tissue collagen. The application of electroactive hydrogel to the skin of the rat was enhanced with respect to the concentration. The Hydroxyproline content level by using GAP-PVA was found to be (1.89 ± 0.10 μg/mg dry tissue) as contents to the (1.52 ± 0.09 μg/mg dry tissue) and (1.67 ± 0.11 μg/mg dry tissue) noted in control rat and Tegaderm treated rat after 15 days of treatment. However, GATP-PVA exhibited significantly ($p < 0.05$) increased hydroxyproline content (2.13 ± 0.12 μg/mg of dry tissue) after 15 days of treatment as compared to control rats (Table 4). An adequate amount of hydroxyproline (amino-acid) is necessary during the early wound healing process to secrete type III collagen to give strength and support the extra-cellular tissue matrix and increase the rate of wound healing. In the maturation process and as the most prevalent collagen in healthy skin, type I collagen is known as essential. Collagen synthesis, deposition, and breakdown are remarkable activities that take place during the whole epidermal healing process. Recent research showed that utilizing cross-linked PVA hydrogel-based biomaterials as an efficient wound dressing material causes a significant rise in the hydroxyproline content of up to two times.

Table 4. Hydroxyproline Content in the Wound Regions of the Experimental Rats

treatment groups	hydroxyproline content (μg/mg of dry tissue)		
	day 05	day 10	day 15
control	0.83 ± 0.11^{b}	1.13 ± 0.05^{b}	1.52 ± 0.09^{b}
tegaderm	1.28 ± 0.06^{a}	1.55 ± 0.14^{a}	1.67 ± 0.11^{a}
GAP-PVA	1.33 ± 0.08^{a}	1.53 ± 0.11^{a}	1.89 ± 0.10^{a}
GATP-PVA	1.53 ± 0.08^{a}	1.72 ± 0.15^{a}	2.13 ± 0.12^{a}

Data are expressed as mean ± SD ($n = 3$). Different superscript letters in the column represent significant differences at ($a > b$; $p < 0.05$). Control (DMSO-treated group), Tegaderm, GAP-PVA (treated group), and GATP-PVA (treated group), respectively.

6. CONCLUSIONS

In this study, a multifunctional hydrogel scaffold was prepared by the coordinative cross-linking of thiolated silver GAT core PANI shell, cross-link with PVA and characterized them for morphological, physio-mechanical, viscoelastic, degradation, cytocompatibility, and biological properties. The in vitro experiment confirmed that these hydrogels exhibited excellent antibacterial activity and free radical scavenging capacities, which are beneficial to enhancing the wound healing process. Furthermore, GATP-PVA hydrogels also showed a significant hemostatic effect, adhesiveness, self-healing ability, tunable gelation time, stiffness, conductivity, water absorption, swelling ratios, and stable rheological properties. In vivo studies further verified that wounds treated with GATP-PVA hydrogels displayed better re-epithelization, granulation thickness, and aligned collagen deposition as compared to gauze-covered wounds and commercial dressing (Tegaderm). Especially, histomorphological evolution and higher concentration of hydroxyproline content during the wound healing process demonstrate the better-promoting effects of these multifunctional hydrogels in the process of vivo wound curing in a full-

https://doi.org/10.1021/acsomega.3c04135
ACS Omega 2023, 8, 39110−39134

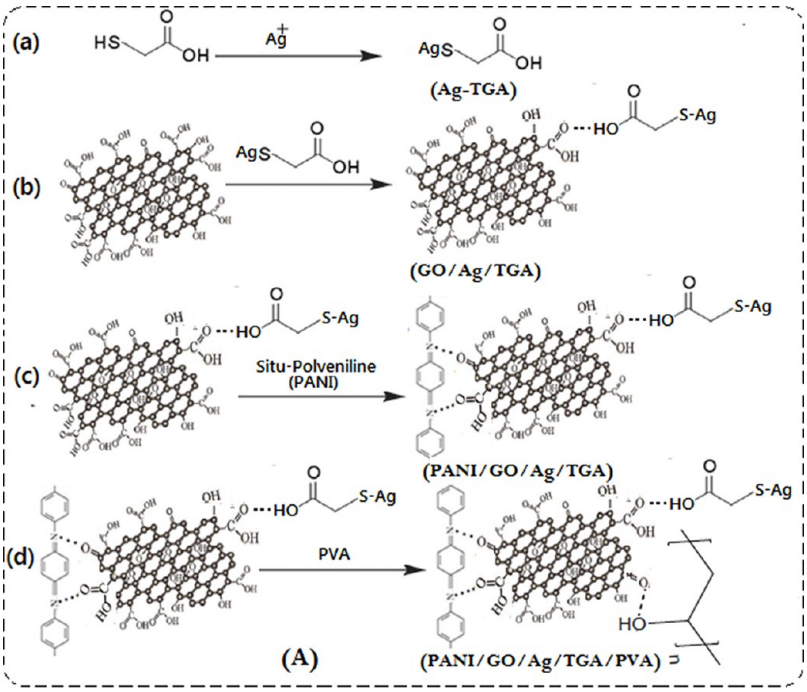

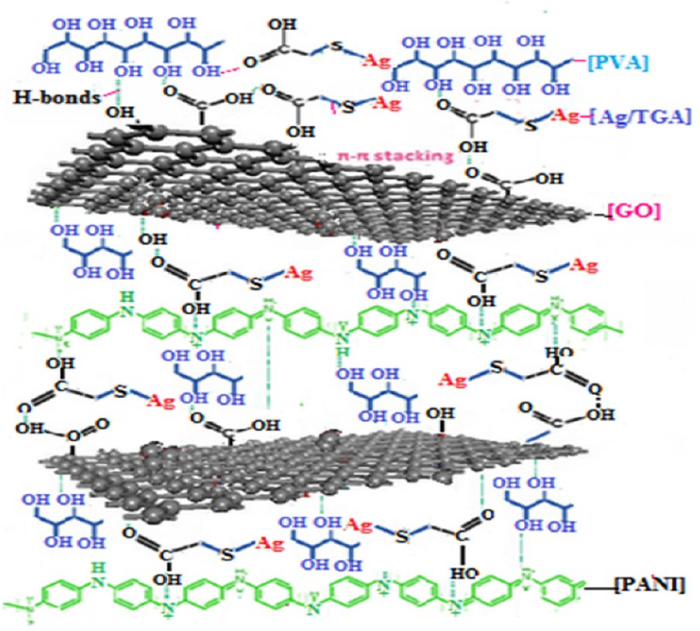

(B)

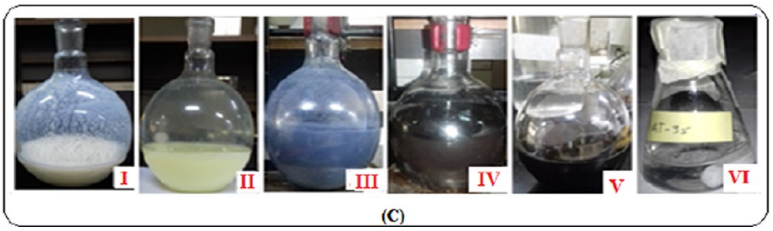

(C)

Figure 22. Schematic representation of the GATP-PVA hydrogel synthesis. (A) Reaction pathway for the synthesis of PANI-coated GAT nanocomposites and GATP-PVA (a), (B) Proposed model which showed adsorption orientation and interactional mechanism of dehydrogenated TGA molecule chemisorbed on GAT along with PANI and PVA. (dotted lines represent hydrogen bonding, $\pi-\pi$ interactions, and electrostatic interactions between different molecules of hydrogels). (C) Color change during synthesis, (I–II) represent a milky solution of TGA and light yellow of Ag NPs/TGA, (III–IV) GAT solution, (V) situ polymerization of PANI on the GAT surface, and (VI) cross-link of PVA with GATP nanocomposites.

https://doi.org/10.1021/acsomega.3c04135
ACS Omega 2023, 8, 39110−39134

thickness mouse skin wound model. The cytocompatibility study of the hydrogels did not show any toxic effects upon contact with fibroblast cells. Additionally, excellent tissue adhesion, fabulous stretching, bending, flexibility, and compression properties also make these hydrogels more favorable in the application of wound dressing. Significant improvements in Young's modulus, glass transition temperature, storage modulus, and tensile strength endorsed strong nanofiller matrix interfacial adhesion. Since electrical stimulation of endogenous electric field at the wound site plays a major role in the wound healing and regeneration process, additional experimental and clinical research is needed to elucidate how wound regeneration is affected by the selection of electroactive hydrogel in healing response with a possible mechanism involving regulation of cell differentiation, cell migration, and tissue growth. These novel hydrogels are inexpensive, environmentally friendly, nontoxic, versatile, scalable, and easily prepared. All these results demonstrated that self-healing electroactive hydrogels with multifunctional properties are ideal candidates as wound dressings for cutaneous skin wound healing involving bacterial infections.

7. MATERIALS AND METHODS

7.1. Materials. All the chemicals used for in situ polymerization synthesis of polyaniline nanocomposites including graphite flake (Sigma-Aldrich 99.99%), silver nitrate (Ag-NO_3 99.98%), sodium borohydride ($NaBH_4$), ammonium peroxydisulfate (APS 99.98%), potassium permanganate ($KMnO_4$ 99.97%), and sodium nitrate (NaNO3 98.99%) were purchased from Sigma Aldrich. Aniline (An, 99%, Sigma-Aldrich) of analytical grade purified by double distillation under N_2 (g) atmosphere and stored at 5 °C before use. Poly(vinyl alcohol) powder (fully hydrolyzed, M_w = 70,000−100,000; Sigma-Aldrich, St. Louis, MO, USA), sodium hydroxide (NaOH 99.98%), 1,1-diphenyl-2-picrylhdrazyl radical (DPPH 99.97%), thioglycolic acid ($C_2H_4O_2S$·98 wt %), and other reagents were of analytical grade and used without further purification (purchased from Merck and Sigma-Aldrich). Solvents of analytical grades such as ethanol, acetone (EtOH), methanol (MeOH), tetrahydrofuran (THF), hydrogen peroxide (H_2O_2 99.98%), sulfuric acid (H_2SO_4 98.00%), nitric acid (HNO_3 67.5%), hydrochloric acid (HCl 36.5%), and phosphate-buffered saline (PBH, PH 7.4) were obtained from Gibco BRL (Carlsbad, CA and Merck Chemicals. Bacterial Strain including MDR *E. coli* (52321), *P. aeruginosa* (27583), and *S. aureus* (6301) were purchased from Biocom Co., Japan. For cell culture, Dulbecco's modified Eagles Medium (high glucose) fetal bovine serum and trypsin were obtained from Gibco BRL (Carlsbad, CA), and double distilled water was used for the preparation of aqueous solution having a resistivity of 18.2MX.

7.2. Synthesis of GO Nanoparticles. GO nanoparticles were produced from pure graphite powder by using the modified Hummers method. In this method, 5 g of graphite powder was added into a mixing solution of sulfuric acid (334 mL) and nitric acid (166 mL) with a 3:1 volume ratio, stirred, and refluxed at 120 °C for 10 h. Then, 4.34 g of potassium permanganate ($KMnO_4$) and 1 g of sodium nitrate ($NaNO_3$) were slowly added into the solution and stirred for 8 h until the solution became dark green. Subsequently, 5 mL of hydrogen peroxide (H_2O_2, 30%) was added to the mixture at 50 °C and stirred for 6 h. Finally, 10 mL of hydrochloric acid (HCl) and 40 mL of distilled water were added, and centrifuge of the reaction mixture was at 4000 rpm for 20 min, washed repeatedly with distilled water, and recentrifuged until a PH-7.0 was achieved. The purified GO was dried under a vacuum to give gold colored solid.

7.3. Synthesis of GO/Ag/TGA (GAT) Nanocomposites. Silver nanoparticles (Ag NPs) were directly deposited on the surface of GO using an aqueous solution of $AgNO_3$ and $NaBH_4$ as reductants in the presence of thioglycolic acid (TGA) to form GO/Ag-TGA (GAT) nanocomposites. For the preparation of the starting material, the routes followed are shown in Figure 21A. Initially, silver nitrate ($AgNO_3$) solution (A) of 50 mM (2.12 g) in 250 mL of distilled water was prepared. Thioglycolic acid of 50 mM (0.5 g) in 100 mL of DI water solution was added to the solution (A) and kept the solution in an ultrasonic bath for 30 min at room temperature. After the formation of small white clusters through the addition of TGA after 5 min solution of Ag-NO_3 changes from transparent to blurry white in color, which confirms the formation of the Ag−S bond. The GO solution of 1 g (0.2 mg/mL) dispersed in 100 mL of water was gradually added to the solution (A) dropwise followed by the gradual addition of 10 mL of $NaBH_4$ (2.0 g/L) under vigorous stirring for 8 h. Finally, a dark brown colloid of (GAT) nanocomposites was obtained. The solution was kept overnight to get a clear light yellow layer of water and precipitate formed by the rotation of 1200 rpm for 20 min and finally washed with distilled water and then centrifuged 3−5 times until the pH = 7 was obtained. It was dried at 50 °C for 24 h, and fine black powder was obtained which was used for further experiment.

7.4. Synthesis of GO/Ag/TGA/PANI (GATP) Nanocomposites. The GATP was prepared by in situ chemical oxidation polymerization of the aniline monomer in the presence of a GAT colloidal solution. In a typical synthesis of GATP nanocomposites, 5 g of aniline monomer in 15 mL of 1 M HNO_3 was put down to 100 mL of GAT dispersion (0.5 mg/mL) in HNO_3 and stirred for 4 h at −2 °C. A solution of dodecyl sulfate (SDS) of 5 g was added as a surfactant. Afterward, to initiate polymerization, 3.97 g (0.8M) of ammonium persulfate (APS) in 20 mL of 1 M HNO_3 was added drop by drop to the above micellar medium over a period of 30 min with continuous stirring. The final mixture was continuously stirred for an additional 24 h in an ice bath. A dark green appearance is an indicator of the formation of GATP nanocomposites. The solution was kept overnight, washed with 1:1 methanol/HCl mixture to remove the unreacted aniline and acid impurities, and then washed with dist. water three times and dried at 40 °C for 24 h in a vacuum oven.

7.5. Synthesis of the GO/Ag/TGA/PANI−PVA (GATP-PVA) Hydrogel. The PVA-based hydrogel was prepared through ordinary mixing of a solution and a cyclic freezing−thawing method as reported previously. First, 5 g of PVA (M_w = 70,000−100,000) was dissolved in 50 mL of distilled water and stirred for 3 h at 70 °C under a boiling water bath, respectively. Subsequently, 1.5 g of GATP was dispersed in 10 mL of distilled water and ultrasonicated for 30 min. The GATP solution was mixed with 50 mL of aqueous PVA solution and stirred vigorously for 30 min, which resulted in the absorption of nanocomposites inside the PVA network and the formation of a uniform swollen hydrogel. Next, the gel is poured into Petri dish and stored at 4 °C in an incubator for 24 h before experimentation (Figure 22).

8. MATERIAL CHARACTERIZATION

The absorption spectrum of the nanocomposites was recorded using a UV−vis spectrophotometer (Shimadzu Japan, UV 2550)

https://doi.org/10.1021/acsomega.3c04135
ACS Omega 2023, 8, 39110−39134

at 30 °C in the wavelength of 200−800 nm for each sample and confirms the formation of nanocomposites. To study the material crystallinity, X-ray diffraction analysis (XRD) was performed in an X-ray diffractometer (Bruker AXS GmBH, Karlsruhe Germany) using Cu Kα radiation ($\lambda = 0.154249$). The diffraction angle (2θ) values were recorded between 10−80° with continuous mode at a scan rate of 0.5/min at a constant temperature of 20 ± 1 °C. FTIR spectra of all the synthesized NCs were simulated through the FT-IR spectrophotometer (PerkinElmer (Waltham, MA, USA) at room temperature. The samples were tested in the form of potassium bromide (KBr) pellets with a scanning range of 400−4000 cm^{-1}. The TGA analyses of the nanocomposites were performed using a thermogravimetric analyzer (TA Instrument, TGA-2050), under a nitrogen atmosphere from 25 to 800 °C through constant heating at the rate of 10 °C/min. SEM (JEOL and JSM-6701, Tokyo and Japan) was used to examine the surface morphology of the samples. The samples were coated on the platinum tape held in a sample holder, and SEM was operated at 10 kV acceleration voltage with an average working distance of 6 mm. TEM (Hitachi H-7500) was used to investigate the size and morphology of the dispersed nanocomposites. Cyclic voltammetry (CV) was measured using a reference 600 Potentiostat/Galvanostat/ZRA (Gamry instrument the hydrogel was coated onto the glassy carbon electrode (GCE) and then the hydrogel film was dried at 55 °C before use. A 3-electrode system using a GCE-coated hydrogel film electrode was used as a working electrode, a Platinum wire used as the auxiliary electrode, and Ag/AgCl as the reference electrode was employed. The test was conducted in 1 molar HCl solution, and the electrochemical test was performed in the potential range from −0.2 V to 1.0 V s and scan rate 50 mV s^{-1}. The electrical conductivity/resistance of the hydrogel was measured using a four-point probe, and the voltage scan range was from −5 to 5 V.

8.1. Self-Healing Properties of the Hydrogel. The self-healing property of the synthesized gel was investigated through a tear-heal test. The columnar hydrogel (GATP-PVA) having 1 cm diameter and 2 cm length was prepared. First, the hydrogel was divided into two pieces, and then, these pieces were brought into contact with each other in phosphate-buffer (PBS, PH 7.4) solution for a period of 2 min at 25 °C and then allowed for self-healing into a columnar hydrogel without any external force. For ease of visualization, the hydrogel was dyed black and white by soaking then in PBS containing 0.002% (wt/vol) ruthenium black dye. The self-healed hydrogel supported the weight itself, and boundaries between the hydrogel pieces became blurred. Furthermore, the healed columnar gel can be removed by lifting over one end of the gel (Figure 7). The healed columnar remains unbroken when the hydrogel is put in a U-shape and stretched. All of the phases of the gel were saved through photography.

8.2. Adhesive Strength Test of the Hydrogel. The adhesive strength of the polymer hydrogel was evaluated using a bovine skin model employing a lap shear test. Bovine skins of 10 × 10 mm^2 bonding area were used as the substrate and fibrin glue was added as the control bioadhesive. The test sample was applied on the dermal side of the skin, and another dermal layer was placed above the first one and allowed to cure. In order to calculate the adhesive strength by applying the force required to remove two various layers, a load of 100 g/cm^2 was applied for 50 min, and adhesive force was calculated by employing a lap shear test, respectively.

8.3. Rheological Experiments. Rheological phenomena of the hydrogel were performed by employing an MCR-301 rheometer (Anton Paar) having parallel plates of 25 mm in diameter and a 0.5 mm gap between the plates. The hydrogels were placed between two parallel plates having 10% strain at a constant temperature of 37 °C. In order to prevent the water evaporation, silicon oil was placed around the hydrogel. The transition from sol to gel is observed through G' (storage modulus) and G'' (loss modulus) as a function of frequency sweep and strain sweep, respectively.

8.4. Initial Moisture Content and Swelling Behavior of the Hydrogel. The degree of swelling and moisture content of the prepared hydrogel was calculated by following the ASTM D570 method.[33] The hydrogel was weighed (W_i) just after the freeze−thaw process. To determine the swelling behavior of the hydrogel sample, it was dried initially at 60 °C for 72 h, allowed to cool in a desiccator, and weighed after cooling (W_d). The hydrogel then emerged in water and kept for 24 h at room temperature. The swollen hydrogel was periodically removed, dried with a lint-free cloth or filter paper, and weighed (W_f). The measurements were continued until a constant weight was achieved for each sample. Finally, the initial moisture content and swelling percentage were calculated using

$$\text{Initial moisture content}(\%) = (W_i - W_d)/W_i \times 100$$

$$\text{Swelling ratio}(\%) = (W_f - W_d)/W_d \times 100$$

where W_i is the initial mass after the completion of the reaction, W_d is the dried mass of the sample in an oven, and W_f is the final weight of the prepared sample after water exposure. Three determinations were performed for each film to obtain an average value.

8.5. Rapid Gelation Time. The vital tilting method was used to note down the gelation time of the hydrogels. The hydrogel was added into a vial with a diameter of 2 cm and placed at 37 °C. The state of the hydrogel was noted down by applying the condition when there was no follow-up observation within minutes by changing the position of the vials, and finally, the experiments were repeated three times to reduce the error in the readings.

8.6. Tensile Properties of the Hydrogel. The tensile strength of the hydrogel was carried out by using a universal tensile tester machine (Instron 5967 USA) at a deformation rate of 50 mm/min and a push−pull force gauge with a clamp distance of 2 cm. Before tensile strength measuring, the rectangular sample (1 × 4 cm^2) was conditioned with saturated solution (52% RH) of Mg $(NO_3)_2$ at room temperature. After equilibration, the tensile strength at break was measured in at least six duplicates for each formula, and the results were evaluated from tensile curves.

9. ANTIBACTERIAL ACTIVITY EVALUATION

The antibacterial activities of the synthesis hydrogel were evaluated against different multidrug resistance bacteria such as *E. coli* (52321), *P. aeruginosa* (27583), and *S. aureus* (6301) via the paper disk diffusion method. In brief, 15 mL (0.04 g/mL) of Muller Hinton agar (MHA) sterilized in an autoclave at a temperature of 12 °C was prepared into a Petri dish, and 100 μL of suspension containing 108 CFU/ml of bacteria of our interest was added in the Petri dish (10 × 90 mm^2) containing MHA.[34] The concentration of 10 μL (200 μg/disc) of the hydrogel was sterilized and impregnated on the 6 mm^2 paper disc, and the zone of inhibition was determined in mm^2.

https://doi.org/10.1021/acsomega.3c04135
ACS Omega 2023, 8, 39110−39134

10. ANTI-OXIDANT ACTIVITY ASSAY PROTOCOL

The free radical scavenging efficiency of the hydrogel was assessed through their reaction with stable 1,1-diphenyle-2-picrylhydrazyl (DPPH) radicals using the methodology.[35] The stock solution of DPPH 0.024 mg/mL was diluted by using ethanol to note the absorbance value of 0.908 ± 0.02 measured at 517 nm. Samples in various concentrations of 15.62 to 500 μg/mL are tested, and then, 1 mL of DPPH is added and shaken gently for proper mixing in complete darkness for 20 min; absorbance was noted down at 517 nm by using a UV−vis spectrophotometer (V-530JASCO). In this experiment, ascorbic acid was used as a standard to compare the DPPH activity, and the experiment was repeated three times to obtain the average results. Scavenging of the free radical was calculated by applying the following equation.

$$\text{Scavenging effect}(\%) = [(\text{Absorbance of controle} - \text{Absorbanceof sample})/\text{Absorbance of controle}] \times 100$$

11. WOUND HEALING EXPERIMENTS

To evaluate the wound healing potential of the hydrogels, adult male albino rats weighing 110−140 g were used, and the Morton wound model was applied on the dorsal skin of albino rats. Twenty-four hours before the excision, the dorsal skin was shaved. On the next day, a full-thickness wound of area (2 cm × 1 cm) was created on the back side of each rat under light chloroform anesthesia using a sterile blade according to the method described by Morton and Malone were taken to maintain the aseptic conditions of the experiments. A measuring scale was used to estimate the extent of wound closure in mm^2 on days 0, 5, 10, and 15 respectively. Additionally, the treated bandages were replaced with new ones every day and activity was stored by taking their pictures 0, 5, 10, and 15 with a digital camera.

11.1. Histopathological Study of the Regenerated Tissues. Skin regeneration and inflammation around the wound were evaluated, and granular tissue samples from all groups were collected on the fifth, 10th, and 15th days and preserved immediately in 10% PBS-buffered paraformaldehyde. The preserved samples were further stained through H&E staining for histopathological examination including maturation, re-epithelialization, matrix organization, and cellular infiltration. All the images were recorded using a light microscope.

11.2. Hemostatic Properties of the Hydrogel. The in vivo hemostatic properties of the prepared hydrogel were examined by employing the hemorrhaging liver mouse model. In brief, 130−210 g male Sprague−Dawley mice were divided into 4 groups ($n = 3$), and the mice were anesthetized by the injection of 10% chloral hydrate and fixed into the surgical board. The liver of the mouse was prone to abdominal incisions and the fluid was removed carefully in order to prevent faults during the estimation of the blood weight obtained through the filter paper. A filter paper (preweighted) was placed on a paraffin film beneath the liver and corkboard slightly tilted (30°). In order to induce bleeding from the liver, a 20 G needle at about 30° was used and the test sample was immediately applied at the bleeding site. When bleeding ceases and blood no longer is drawn to the filter paper, stop the watch and weigh the filter paper again with absorbed blood in order to measure and compare with the control group for each rat.

11.3. Cytocompatibility Evaluation of the Hydrogels. The cytocompatibility of the electroactive hydrogel was determined by a cell viability (LIVE/DEAD) assay using L929 fibroblast cells, as described in the literature. The cells were seeded at a density of 4×-10^4 per well into various gels in 24-well plates and tissue culture plastic surface (positive control). An additional 1 mL of the corresponding cell culture medium was added in each well, shaken lightly, and incubated in 5% CO_2 for 48 and 72 h at 37 °C, respectively. After the predetermined period, the incubation medium was removed and the seeded hydrogel was washed with PBS solution; then, 0.05% calcium dye (live staining) and 0.3% ethidium homodimer dye (dead staining) were added to the contents of each well, left to incubate for 60 min, and transferred to a 96-well microliter plate for fluorescence measurement. The fluorescence intensity was measured at emission and excitation wavelengths 530 and 590 nm, respectively, using a Leica DMRX fluorescence microscope (Leica Microsystems Ltd., Milton Keynes, UK). A digital image was obtained using a DS-Qi 1Mc Nikon digital camera (Amsterdam, Netherlands). The cell viability ratio (%) was calculated by using the following formula:

$$\text{Viability}(\%) = (A_{\text{sample}})/(A_{\text{control}}) \times 100\%$$

where A_{sample} and A_{control} are the absorptions at 490 nm for the experimental and control wells, respectively.

11.4. Hydroxyproline Estimations. The most prominent tissue of the collagen is hyroxyproline, which was known as a biochemical marker and quantified according to the Lee and Tong method. Briefly, the wound tissue (0.1 g) was completely dried in hot air at 60−70 °C and then hydrolyzed in 6 M HCl (100 μL HCl/mg dry tissue) for 3 h at 110 °C in a sealed glass tube. The pH of the hydrolysates was adjusted to 7.0 by adding 500 μL of 5 M NaOH solution. After this, 10 μL of the test sample was loaded into the 96-well plates followed by the addition of 90 μL of chloramine-T solution (0.053 M) and incubated at room temperature (60 °C) for 20 min. Absorbance was recorded at 557 nm via a microplate reader, and the hydroxyproline content was calculated from the linear standard curve and presented as μg/mg of dry tissue weight.

11.5. Statistical Analysis. All the experiments were executed in triplicate ($n = 3$), and the results were presented as mean ± SD (standard deviation). LD_{50} and IC_{50} values were analyzed by using the standard student t test, and Statistic software 8.1 was used to examine the "p" values smaller or equal ($p \leq 0.05$) as the criterion for a statistically significant difference among the sample.

AUTHOR INFORMATION

Corresponding Author

Wajid Rehman − *Department of Chemistry, Hazara University, Mansehra 21120, Pakistan;* orcid.org/0000-0003-0128-0377; Phone: 0092-333-5779831; Email: sono_waj@yahoo.com

Authors

Asghar Khan − *Department of Chemistry, Hazara University, Mansehra 21120, Pakistan*

Mohammed M. Alanazi − *Department of Pharmaceutical Chemistry, College of Pharmacy, King Saud University, Riyadh 11451, Saudi Arabia*

Yaqoob Khan − *Nano Science and Technology Department, National Centre for Physics, Quaid-I-Azam University, Islamabad 44000, Pakistan*

https://doi.org/10.1021/acsomega.3c04135
ACS Omega 2023, 8, 39110−39134

Liaqat Rasheed − *Department of Chemistry, Hazara University, Mansehra 21120, Pakistan*
Abdul Saboor − *Department of Chemistry, Hazara University, Mansehra 21120, Pakistan*
Shahid Iqbal − *School of Chemical and Environmental Engineering, College of Chemistry, Chemical Engineering and Materials Science, Soochow University, Suzhou, Jiangsu 215123, China*

Complete contact information is available at: https://pubs.acs.org/10.1021/acsomega.3c04135

Author Contributions

Methodology: A.K.; Concept, supervision, Manuscript draft: W.R.; Formal analysis. Funding: M.M.A.; Data curation, visualization, cosupervision; Y.K., Resources: L.R.; Manuscript editing, Software: A.S.; Formal Analysis, Visualization: S.I.

Author Contributions

We have obeyed the Ethical Guidelines for the Animal Studies. The transgenic animals of either sex (Mo/HuAPP695swe/Swedish mutations K595N/M596) were procured from the Jackson Laboratory [Bar Harbor, USA; strain name B6C3Tg (APPswe, PSEN 1dE9). All the experimental procedures were permitted by Ethical Committee vide ref. No. DREC/20200405/06 of the Department of Pharmacy, University of Swabi, Pakistan. After the experimental procedures, the animals were euthanized properly as per the standard procedure using AVMA Guidelines for the Euthanasia of Animals. Halothane vapors were slowly given to the animals to induce anesthesia. The overdose and prolong time euthanized the animals.

Notes

The authors declare no competing financial interest.

■ ACKNOWLEDGMENTS

The authors extend their appreciation to the Researchers Supporting Project number (RSPD2023R628), King Saud University, Riyadh, Saudi Arabia, for funding this research.

■ REFERENCES

(1) Zhao, X.; Wu, H.; Guo, B.; Dong, R.; Qiu, Y.; Ma, P. X. Antibacterial anti-oxidant electroactive injectable hydrogel as self-healing wound dressing with hemostasis and adhesiveness for cutaneous wound healing. *Biomaterials* **2017**, *122*, 34−47.
(2) Han, X.; Meng, G.; Wang, Q.; Cui, L.; Wang, H.; Wu, J.; Liu, Z.; Guo, X. Mussel-inspired in situ forming adhesive hydrogels with antimicrobial and hemostatic capacities for wound healing. *J. Biomater. Appl.* **2019**, *33* (7), 915−923.
(3) Chandika, P.; Ko, S.-C.; Jung, W.-K. Marine-derived biological macromolecule-based biomaterials for wound healing and skin tissue regeneration. *Int. J. Biol. Macromol.* **2015**, *77*, 24−35.
(4) Kamoun, E. A.; Kenawy, E.-R. S.; Chen, X. A review on polymeric hydrogel membranes for wound dressing applications: PVA-based hydrogel dressings. *J. Adv. Res.* **2017**, *8* (3), 217−233.
(5) Zhao, X.; Dong, R.; Guo, B.; Ma, P. X. Dopamine-incorporated dual bioactive electroactive shape memory polyurethane elastomers with physiological shape recovery temperature, high stretchability, and enhanced C2C12 myogenic differentiation. *ACS Appl. Mater. Interfaces* **2017**, *9* (35), 29595−29611.
(6) Fan, Z.; Liu, B.; Wang, J.; Zhang, S.; Lin, Q.; Gong, P.; Ma, L.; Yang, S. A novel wound dressing based on Ag/graphene polymer hydrogel: effectively kill bacteria and accelerate wound healing. *Adv. Funct. Mater.* **2014**, *24* (25), 3933−3943.
(7) Zhao, X.; Guo, B.; Wu, H.; Liang, Y.; Ma, P. X. Injectable antibacterial conductive nanocomposite cryogels with rapid shape recovery for noncompressible hemorrhage and wound healing. *Nat. Commun.* **2018**, *9* (1), 2784 DOI: 10.1038/s41467-018-04998-9.
(8) Shi, Z.; Gao, X.; Ullah, M. W.; Li, S.; Wang, Q.; Yang, G. Electroconductive natural polymer-based hydrogels. *Biomaterials* **2016**, *111*, 40−54.
(9) Zhang, H.; Zhang, J.; Peng, X.; Li, Z.; Bai, W.; Wang, T.; Gu, Z.; Li, Y. Smart Internal Bio-Glues. *Adv. Sci.* **2022**, *9* (27), No. 2203587, DOI: 10.1002/advs.202203587.
(10) Kost, J.; Langer, R. Responsive polymeric delivery systems. *Adv. Drug Deliv. Rev.* **2012**, *64*, 327−341.
(11) Kabir, S. F.; Sikdar, P. P.; Haque, B.; Bhuiyan, M. R.; Ali, A.; Islam, M. Cellulose-based hydrogel materials: Chemistry, properties and their prospective applications. *Prog. Biomater.* **2018**, *7*, 153−174.
(12) Ray, S.; Saha, A.; Basiruddin, S.; Roy, S.; Jana, N. R. Polyacrylate-coated graphene-oxide and graphene solution via chemical route for various biological application. *Diam. Relat. Mater.* **2011**, *20* (3), 449−453.
(13) Tavakoli, J.; Tang, Y. Honey/PVA hybrid wound dressings with controlled release of antibiotics: Structural, physico-mechanical and in-vitro biomedical studies. *Mater. Sci. Eng.: C* **2017**, *77*, 318−325.
(14) Zhang, H.; Xia, H.; Zhao, Y. Poly (vinyl alcohol) hydrogel can autonomously self-heal. *ACS Macro Lett.* **2012**, *1* (11), 1233−1236.
(15) Dehbari, N.; Tavakoli, J.; Khatrao, S. S.; Tang, Y. In situ polymerized hyperbranched polymer reinforced poly (acrylic acid) hydrogels. *Mater. Chem. Front.* **2017**, *1* (10), 1995−2004.
(16) Mahanta, N.; Teow, Y.; Valiyaveettil, S. Viscoelastic hydrogels from poly (vinyl alcohol)−Fe (iii) complex. *Biomater. Sci.* **2013**, *1* (5), 519−527.
(17) Gizdavic-Nikolaidis, M.; Ray, S.; Bennett, J. R.; Easteal, A. J.; Cooney, R. P. Electrospun functionalized polyaniline copolymer-based nanofibers with potential application in tissue engineering. *Macromol. Biosci.* **2010**, *10* (12), 1424−1431.
(18) Guo, B.; Ma, P. X. Synthetic biodegradable functional polymers for tissue engineering: a brief review. *Sci. China Chem.* **2014**, *57*, 490−500.
(19) Athukorala, S. S.; Tran, T. S.; Balu, R.; Truong, V. K.; Chapman, J.; Dutta, N. K.; Roy Choudhury, N. 3D printable electrically conductive hydrogel scaffolds for biomedical applications: A review. *Polymers* **2021**, *13* (3), 474.
(20) Hsieh, F.-Y.; Tseng, T.-C.; Hsu, S.-H. Self-healing hydrogel for tissue repair in the central nervous system. *Neural Regen. Res.* **2015**, *10* (12), 1922.
(21) Shin, S. R.; Jung, S. M.; Zalabany, M.; Kim, K.; Zorlutuna, P.; Kim, S. B.; Nikkhah, M.; Khabiry, M.; Azize, M.; Kong, J. Carbon-nanotube-embedded hydrogel sheets for engineering cardiac constructs and bioactuators. *ACS Nano* **2013**, *7* (3), 2369−2380.
(22) Qu, J.; Zhao, X.; Liang, Y.; Xu, Y.; Ma, P. X.; Guo, B. Degradable conductive injectable hydrogels as novel antibacterial, anti-oxidant wound dressings for wound healing. *Chem. Eng. J.* **2019**, *362*, 548−560.
(23) Guo, B.; Qu, J.; Zhao, X.; Zhang, M. Degradable conductive self-healing hydrogels based on dextran-graft-tetraaniline and N-carboxyethyl chitosan as injectable carriers for myoblast cell therapy and muscle regeneration. *Acta Biomater.* **2019**, *84*, 180−193.
(24) Goudarzi, I.; Hajizadeh, S.; Salmani, M. E.; Abrari, K. Pulsed electromagnetic fields accelerate wound healing in the skin of diabetic rats. *Bioelectromagnetics* **2010**, *31* (4), 318−323.
(25) Nuccitelli, R.; Nuccitelli, P.; Li, C.; Narsing, S.; Pariser, D. M.; Lui, K. The electric field near human skin wounds declines with age and provides a noninvasive indicator of wound healing. *Wound Repair Regen.* **2011**, *19* (5), 645−655.
(26) Pearce, J. *Luigi Galvani: beginnings of electrophysiology*; JMS 2019.
(27) Thakral, G.; LaFontaine, J.; Najafi, B.; Talal, T. K.; Kim, P.; Lavery, L. A. Electrical stimulation to accelerate wound healing. *Diabet. Foot Ankle* **2013**, *4* (1), 22081.
(28) Liu, Y.; Wang, P.; Su, X.; Xu, L.; Tian, Z.; Wang, H.; Ji, G.; Huang, J. Electrically programmable interfacial adhesion for ultrastrong hydrogel bonding. *Adv. Mater.* **2022**, *34* (13), No. 2108820, DOI: 10.1002/adma.202108820.

(29) Guo, B.; Glavas, L.; Albertsson, A.-C. Biodegradable and electrically conducting polymers for biomedical applications. *Prog. Polym. Sci.* **2013**, *38* (9), 1263−1286.
(30) Chen, J.; Yu, M.; Guo, B.; Ma, P. X.; Yin, Z. Conductive nanofibrous composite scaffolds based on in-situ formed polyaniline nanoparticle and polylactide for bone regeneration. *J. Colloid Interface Sci.* **2018**, *514*, 517−527.
(31) Zhang, M.; Guo, B. Electroactive 3D scaffolds based on silk fibroin and water-borne polyaniline for skeletal muscle tissue engineering. *Macromol. Biosci.* **2017**, *17* (9), No. 1700147.
(32) Zhang, X.; Qi, H.; Wang, S.; Feng, L.; Ji, Y.; Tao, L.; Li, S.; Wei, Y. Cellular responses of aniline oligomers: a preliminary study. *Toxicol. Res.* **2012**, *1* (3), 201−205.
(33) Biduski, B.; da Silva, W. M. F.; Colussi, R.; El Halal, S. L. D. M.; Lim, L.-T.; Dias, Á. R. G.; da Rosa Zavareze, E. Starch hydrogels: The influence of the amylose content and gelatinization method. *Int. J. Biol. Macromol.* **2018**, *113*, 443−449.
(34) Pandiyarajan, T.; Udayabhaskar, R.; Vignesh, S.; James, R. A.; Karthikeyan, B. Synthesis and concentration dependent antibacterial activities of CuO nanoflakes. *Mater. Sci. Eng.: C* **2013**, *33* (4), 2020−2024.
(35) Le Thi, P.; Lee, Y.; Tran, D. L.; Thi, T. T. H.; Kang, J. I.; Park, K. M.; Park, K. D. In situ forming and reactive oxygen species-scavenging gelatin hydrogels for enhancing wound healing efficacy. *Acta Biomater.* **2020**, *103*, 142−152.

https://doi.org/10.1021/acsomega.3c04135
ACS Omega 2023, 8, 39110−39134